NANO · MICRO small
www.small-journal.com

Advancements and Challenges in the Integration of Indium Arsenide and Van der Waals Heterostructures

Tiantian Cheng, Yuxin Meng, Man Luo, Jiachi Xian, Wenjin Luo, Weijun Wang, Fangyu Yue, Johnny C. Ho,* Chenhui Yu,* and Junhao Chu*

The strategic integration of low-dimensional InAs-based materials and emerging van der Waals systems is advancing in various scientific fields, including electronics, optics, and magnetics. With their unique properties, these InAs-based van der Waals materials and devices promise further miniaturization of semiconductor devices in line with Moore's Law. However, progress in this area lags behind other 2D materials like graphene and boron nitride. Challenges include synthesizing pure crystalline phase InAs nanostructures and single-atomic-layer 2D InAs films, both vital for advanced van der Waals heterostructures. Also, diverse surface state effects on InAs-based van der Waals devices complicate their performance evaluation. This review discusses the experimental advances in the van der Waals epitaxy of InAs-based materials and the working principles of InAs-based van der Waals devices. Theoretical achievements in understanding and guiding the design of InAs-based van der Waals systems are highlighted. Focusing on advancing novel selective area growth and remote epitaxy, exploring multi-functional applications, and incorporating deep learning into first-principles calculations are proposed. These initiatives aim to overcome existing bottlenecks and accelerate transformative advancements in integrating InAs and van der Waals heterostructures.

1. Introduction

For decades, shrinking transistors have been crucial to the progress of semiconductor chip technology; for 5 nm nodes and beyond, complex quantum effects begin to dominate the performance of semiconductor devices, which makes it unreliable to apply the traditional device structures and physics based on the drift–diffusion models.[1–3] For example, the localized effects induced by shrinking detector dimensions resulted in unprecedented responsivity and electrical transport amplification enhancement, marking a significant departure from conventional photoelectric conversion mechanisms and device response behaviors.[4] Van der Waals (vdW) materials and devices, distinguished by their capability to precisely manipulate geometric structures and physical properties at the single-atomic-layer dimension, have recently attracted considerable research interest in fostering the development of semiconductor chip technologies.[5–9] Particularly, vdW heterostructures relax the constraints on lattice matching and process compatibility imposed by traditional bulk materials with covalent bonds, which enable the boundless integration of various heterogeneous and mixed-dimensional vdW structures, ranging from quantum dots (QDs), 1D nanowires (NWs), 2D nanosheets, to 3D bulk materials.[10–12] They have atomically flat heterojunction interfaces, weak interlayer vdW interactions, and flexible multi-material and multi-dimensional stacking configurations, which result in novel physical properties and superior device performance.[13–15]

Current research for vdW systems based on novel 2D layered materials is flourishing, represented by graphene (GN),[16,17] boron nitride (BN),[18] and transition metal dichalcogenides.[19]

T. Cheng, Y. Meng, M. Luo, J. Xian, C. Yu
School of Microelectronics and School of Integrated Circuits
School of Information Science and Technology
Nantong University
Nantong 226019, P. R. China
E-mail: luoman@ntu.edu.cn; ychyu@ntu.edu.cn

The ORCID identification number(s) for the author(s) of this article can be found under https://doi.org/10.1002/smll.202403129

DOI: 10.1002/smll.202403129

M. Luo, W. Wang, J. C. Ho
Department of Materials Science and Engineering and State Key Laboratory of Terahertz and Millimeter Waves
City University of Hong Kong
Hong Kong SAR 999077, P. R. China
E-mail: johnnyho@cityu.edu.hk

W. Luo
Department of Physics and JILA
University of Colorado
Boulder, CO 80309, USA

F. Yue, J. Chu
School of Physics and Electronic Science
East China Normal University
Shanghai 200241, P. R. China

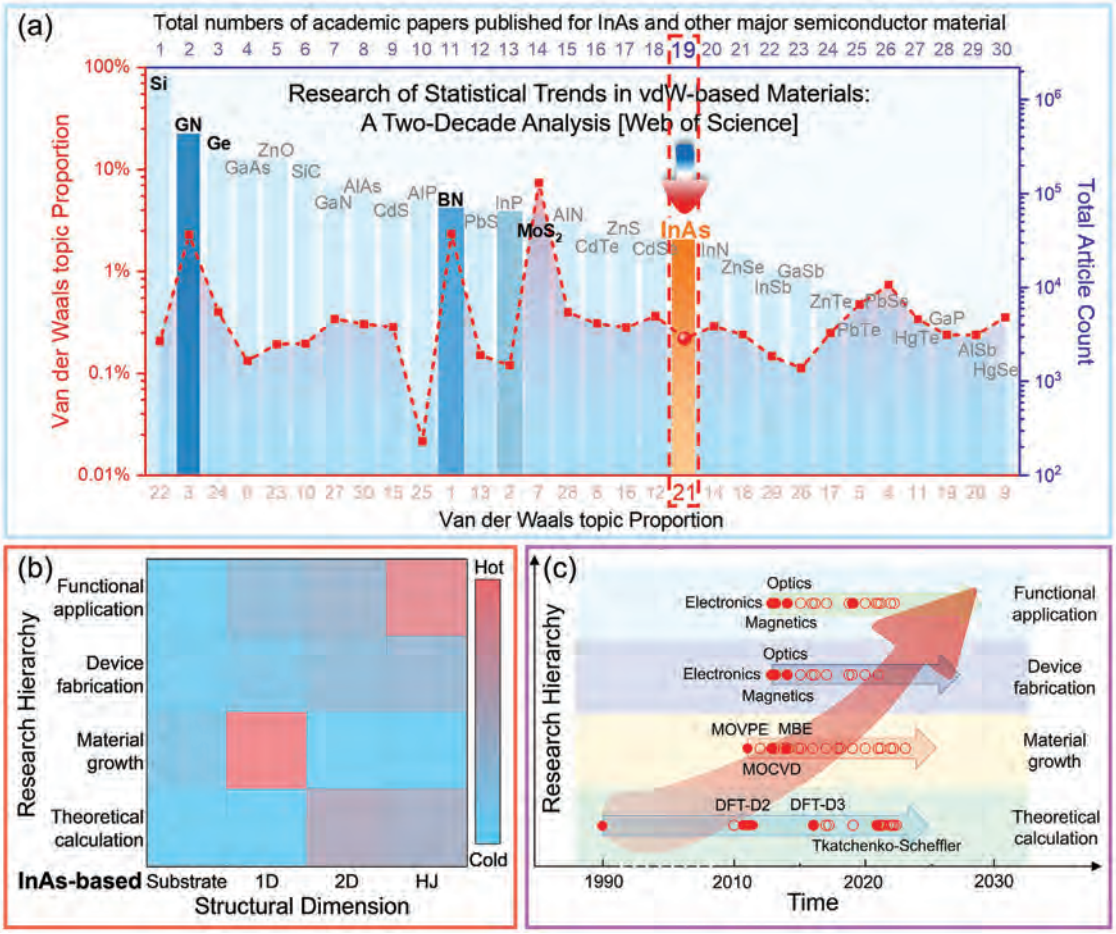

Figure 1. a) Ranking of vdW topic proportions (dashed line) and total numbers (bar chart) of academic papers published for InAs against Si, Ge, novel 2D layered materials (graphene, BN, MoS_2), and other traditional binary compound materials. b) Heatmap analysis of InAs-based vdW research activities, including theoretical calculation, material growth, device fabrication, and functional application. c) Timelines exhibiting the pivotal milestones and recent achievements in the research on InAs-based vdW materials and devices. Web of Science databases updated to June 2024 are referred to in the statistical works here. a)GN: Graphene; b)HJ: Heterojunction.

The research system of these materials is incompatible with traditional semiconductor materials despite their straightforward fabrication processes[20,21] and distinctive physical attributes.[22–25] Exploring these 2D layered materials substantially requires the establishment of new theoretical frameworks and experimental methods rather than relying on existing traditional semiconductor principles and technologies.[26,27] The successful integration of conventional semiconductor materials into vdW systems allows the comprehensive utilization of the advantages of 2D layered materials, facilitating the practical application of the established research framework associated with traditional semiconductor materials. Thus, exploring the vdW topics based on conventional semiconductor materials holds a significant research value.[28–30] The depth and breadth of research related to vdW topics vary for different traditional semiconductor materials, as shown in **Figure** 1a. The concept of the vdW topic proportion for indium arsenide (InAs) and other primary semiconductor materials is introduced to mirror such differences. It refers to the proportion of academic papers on vdW topics in the total number of academic papers published in the past two decades, as indexed in the Web of Science database until June 2024, when this review was completed.

As a crucial member of the III-V semiconductor family, InAs exhibits distinctive physical properties that distinguish it from traditional semiconductors, rendering it essential across various technological domains. In the electronics sector, its superior electron mobility makes InAs ideal for high-frequency and low-power devices.[31–33] In optics, its effective infrared absorption capacity ensures widespread use in highly sensitive photonic and optoelectronic systems.[34–37] In magnetics, the strong spin–orbit interactions (SOI) in InAs are critical for developing spintronic devices for digital storage and quantum computing.[38–40] Furthermore, integrating InAs with vdW materials enhances assembly flexibility due to reduced interface states, improved thermal management, and relaxed lattice mismatch. This integration facilitates the development of novel device architectures, leveraging the unique properties of both InAs and vdW materials. Unfortunately, research targeting InAs-based vdW systems has not achieved the anticipated advancements. Among primary traditional semiconductor materials in Figure 1a, the ranking of the

vdW topic proportions relative to the total article count for InAs declines three places, from 19th to 21st. This decline implies that research on the InAs vdW topic faces the disadvantage of lagging behind other semiconductor materials and technologies.

Research activities on InAs-based vdW topics up to the present stage can be broadly classified into four categories, as visualized by Figure 1b. The hot and cold ends of the color bar represent the intensity of research activity within their indicated categories. Research accomplishments are mainly contributed by the vdW epitaxial growth of InAs NWs and the functional application of InAs-based vdW heterojunctions. In contrast, experimental advances on material growth beyond NWs appear to lag, reflecting the nascent stage of InAs-based vdW research. In fact, the history of research on InAs-based vdW topics is not short. The earliest study dates back to 1989, which considered vdW interactions in examining the mechanical characteristics of InAs.[41] Since then, incorporating InAs-based materials into vdW systems has experienced rapid advancements, as shown in Figure 1c. The research on vdW epitaxial growth of InAs-based materials is of significant interest to the experimental front. Theoretical calculation also starts early and elucidates the intrinsic causes of the physical properties of InAs-based vdW materials and the working mechanisms of InAs-based vdW devices in recent years.[42] Both experimental and theoretical efforts indicate that InAs-based vdW heterojunctions hold vast potential for functional application in various domains.

Several critical experimental techniques and theoretical issues remain to be resolved before significant breakthroughs in the research on InAs-based vdW topics can be achieved. First, the synthesis of pure crystalline phase InAs nanostructures and single-atomic-layer 2D InAs films has yet to be realized; both are the basic building blocks needed for perfect and hybrid InAs-based vdW integrated systems. In addition, the impact of surface states on the performance of InAs-based vdW heterogeneous integrated systems is diverse and uncertain, which complicates the empirical measurements and performance evaluations. It is essential to seek solutions to the above experimental dilemmas by introducing theoretical calculations, which offer a quantitative foundation for directing experimental endeavors in this domain. Unfortunately, the physical models and computational techniques of theoretical research themselves face severe challenges. Detailed discussions about these specific issues and corresponding solutions will be presented in the following review.

The main content of this review is organized as follows. This introduction section outlines the research progress and challenges in integrating traditional semiconductor material InAs into vdW systems. The second section explains fundamental knowledge pertinent to the InAs-based vdW research, including crystal structures of bulk InAs and vdW films, vdW epitaxy and integration techniques, and first-principles calculations (FPC). The third section explores the InAs-based materials grown by vdW epitaxy, covering InAs NWs, NW heterostructures, QDs, and InAs films. Nucleation, growth mechanisms, and effective process optimization of InAs NWs are discussed to provide references for improving their morphology characteristics and crystal quality. The fourth section analyzes the critical role of vdW heterojunctions on the performance of InAs-based vdW integrated devices, such as diodes, transistors, solar cells, photodetectors, and devices integrated with bulk materials. The fifth section emphasizes theoretical achievements in FPC related to InAs-based vdW topics, particularly the quantitative analysis of electrical, optical, and magnetic characteristics of energetically stable InAs-based vdW heterostructures. The last section summarizes the research advances in InAs-based vdW topics from a higher perspective. On this basis, innovative solutions are put forth, including advancing novel selective area growth and remote epitaxy, exploring multi-functional and multi-disciplinary applications, and incorporating deep learning techniques into FPC. These proposals aim to overcome the critical challenges faced in both experimental and theoretical aspects, thereby accelerating the development of strategic integration of InAs and vdW heterostructures.

2. Fundamental Knowledge

In this section, we introduce fundamental knowledge in the InAs-based vdW research. The crystal structures of bulk InAs and vdW films, alongside their vdW epitaxy and integration techniques, are presented. Then, the computational models of FPC, such as density functional theory (DFT) and approximations to the exchange–correlation functional and vdW models, are discussed.

2.1. Crystal Structure

The crystal structures of InAs are determined by the ordered atomic arrangements in the solid, covering both experimentally observed bulk forms and theoretically predicted vdW films.

Bulk InAs manifests hexagonal wurtzite (WZ) and cubic zinc-blende (ZB) crystal structures, each defined by distinct atomic stacking sequences: {0001} WZ as AaBbAaBbAaBb... and {111} ZB as C(c)A(a)B(b)C(c)A(a)B(b)..., as depicted in **Figure 2a**.[43] These configurations typically exhibit axial growth along [0001] and [111], respectively.[44,45] Traditional crystal unit cell structures of InAs are shown in Figure 2b, which correspond to the axial growth along ZB $\langle 1\bar{1}0\rangle$, WZ $\langle 0001\rangle$, and ZB $\langle 111\rangle$.[46] Characterized by strong covalent bonds, bulk InAs has a nonlayered structure and is prone to form stacking faults (SFs) during crystal growth.[47,48]

Monolayer, bilayer, and multi-layer InAs vdW films are theoretically predicted as energetically stable 2D structures. For monolayer InAs, the hexagonal buckled (BK) structure,[49] comprising two parallel but inequivalent atomic layers separated by a vertical buckling distance (Δ), is favored over the planar structure where all atoms align in one plane, as shown in Figure 2c.[50] Other possible monolayer structures receive less attention compared to hexagonal BK structures, such as tetragonal (TETRA),[51] hexagonal zigzag (ZIG),[52] and hexagonal armchairs (ARM).[53] For bilayer InAs, the double honeycomb (DLHC) structure surpasses the stability of single-layer honeycomb or truncated bulk (BT) structures.[54–57] Within the DLHC, each cation connects with three anions from the same layer and one from the adjacent layer, creating a distorted tetrahedral coordination, as shown in Figure 2d.[55] For multi-layer InAs, the haeckelite structure featuring alternating octagonal and square rings emerges as the most energetically favorable.[58]

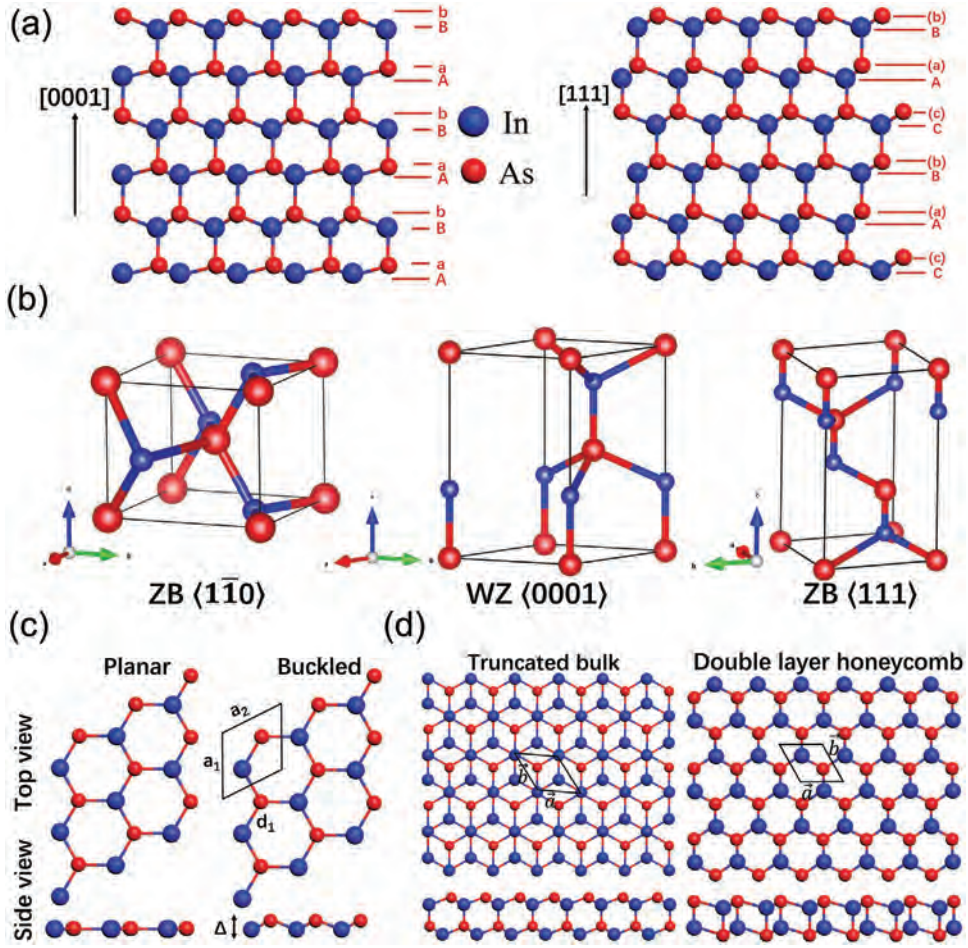

Figure 2. Crystal structures of bulk InAs and vdW films redrawn from references. a) Plane stacking sequences: {0001} in wurtzite structure and {111} in zinc blende structure. Reproduced with permission.[43] Copyright 2013, American Chemical Society (ACS). b) Typical crystal unit cell structures: zinc blende ⟨1$\bar{1}$0⟩, wurtzite ⟨0001⟩, and zinc blende ⟨111⟩ bulk InAs. Reproduced with permission.[46] Copyright 2016, ACS. Energetically stable InAs vdW films predicted by FPC: c) monolayer planar and buckled structures, d) bilayer truncated bulk and double layer honeycomb structures. Reproduced with permission.[50] Copyright 2016, American Physical Society (APS). Reproduced with permission.[55] Copyright 2021, Elsevier.

2.2. VdW Epitaxy and Integration

VdW materials are distinguished from covalent-bonded materials by physical interactions and structural properties. VdW materials exhibit weak vdW interactions, whose intensity is highly dependent on vdW distance, defined as the sum of the vdW gap and the covalent bond length in **Figure 3**a.[11] Besides, vdW materials possess atomically flat interfaces without dangling bonds, easing lattice-matching constraints and boosting electronic transport efficiency.[11] Collectively, these features equip vdW materials with novel physical properties and potential for pioneering device applications.[59–62]

VdW epitaxy alleviates the strict requirements for lattice matching and process compatibility, addressing a longstanding challenge in traditional heterogeneous epitaxy.[63,64] Pure VdW epitaxy and quasi-vdW epitaxy in Figure 3b possess distinct benefits for advanced materials fabrication.[65] While pure VdW epitaxy excels in developing 2D/2D vdW heterostructures, it faces practical challenges.[66] Quasi-vdW epitaxy is a more versatile and feasible approach for integrating pure vdW materials with traditional covalent-bonded materials since vdW interactions can occur on any passivated or dangling-bond-free interfaces, thus enriching diverse vdW structures.[67]

Various growth techniques are applied in fabricating InAs-based vdW materials, such as molecular beam epitaxy (MBE), metal–organic chemical vapor deposition (MOCVD), metal–organic vapor-phase epitaxy (MOVPE), and chemical vapor deposition (CVD). For MOCVD, the diffusion and accumulation dynamics of III-group adatoms on the GR surface are illustrated in Figure 3c,[68] where adatoms disperse toward edges, kinks, or defects within their diffusion length (λ). Thermodynamically, potential adsorption sites for III-group adatoms on carbon honeycomb lattices include the center (H-sites) and the midpoint of carbon–carbon bonds (B-sites), with In atoms theoretically preferring the H-sites.[69–71] Similar basic mechanisms are observed in other growth techniques for InAs vdW material preparation.

VdW integration comes with great freedom and flexibility when designing various heterogeneous and mixed-dimensional vdW stacking configurations.[72–75] This innovative strategy is expected to address persistent barriers in traditional semiconductor

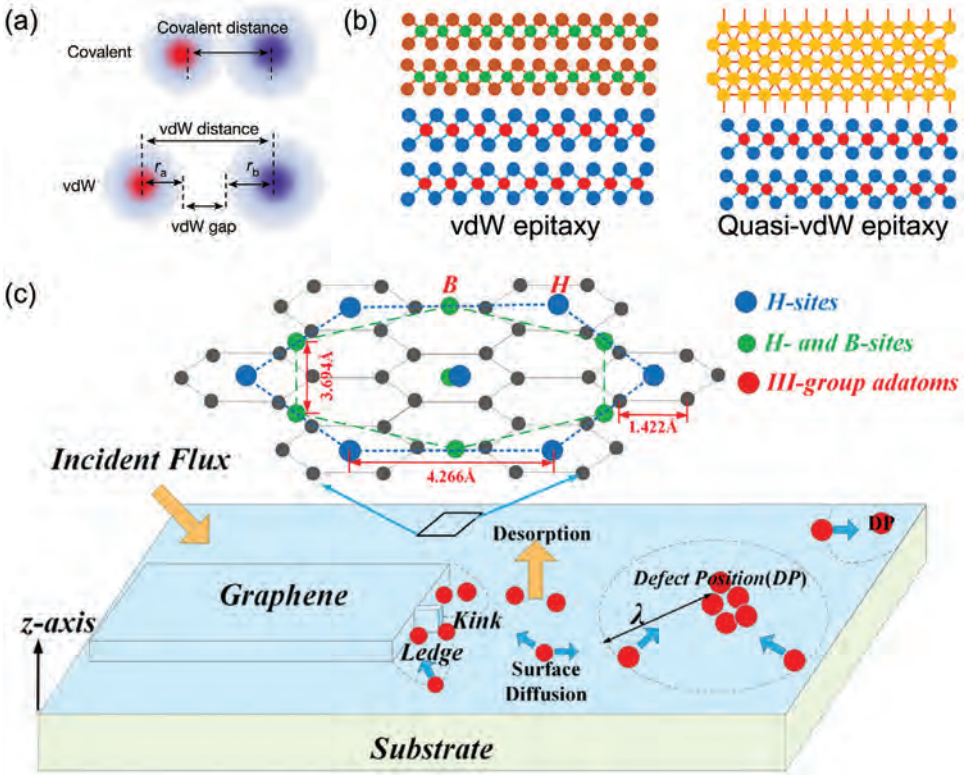

Figure 3. a) Schematic of vdW distance and vdW gap. Reproduced with permission.[11] Copyright 2019, Springer Nature. b) Schematic of vdW and quasi-vdW epitaxy with dangling-bond free vdW interfaces. Reproduced with permission.[65] Copyright 2022, American Institute of Physics (AIP). c) Diffusion and accumulation dynamics of III-group adatoms on graphene films. Inset showing the possible adsorption sites of III-group adatoms: above the center of the carbon honeycomb (H-sites) or midpoint of the carbon–carbon bond bridge (B-sites). Reproduced with permission.[68] Copyright 2023, ACS.

epitaxy, such as lattice mismatch and process incompatibility among semiconductors with differentiated crystal structures, electronic properties, or geometric dimensions.[76–78]

2.3. First-Principles Calculations

FPC is a computational technique that utilizes the fundamental principles of quantum mechanics to explore the intrinsic mechanisms of semiconductor attributes and innovative device functionalities. This section briefly summarizes the computational methodologies and theories of FPC, as tabulated in **Table** 1. The customized implementation of FPC in the InAs-based vdW system will be detailed in Section 5. For an in-depth analysis, readers may refer to our earlier review.[42]

2.3.1. Density Functional Theory

Traditional wave function theory solves the Schrödinger equation using multi-electronic wave functions, whose computational complexity increases tremendously as the number of electrons grows. In contrast, DFT utilizes ground-state electron density as the primary variable, providing a more efficient method for broader applications.[85,86] The Kohn–Sham scheme, an implementation of DFT, predicts ground state properties of multi-electron systems by computing electron density and total energy based on non-interacting spin orbitals, effectively describing electron–electron interactions. Hartree–Fock calculations, another DFT implementation, offer simplicity and efficiency but cannot capture electron correlation effects, leading to inaccuracies in thermochemical reactions and band gap size evaluations.[87]

2.3.2. Approximations to the Exchange–Correlation Functional

The computational cost and accuracy of DFT in conjunction with the Kohn–Sham scheme largely depend on the choice of approximations for the exchange–correlation function.[79] Local density approximation (LDA), generalized gradient approximation (GGA), and Meta-GGA are three progressively refined approximations, each targeting a more exact description of the exchange and correlation effects among electrons. Up to now, Perdew–Burke–Ernzerhof GGA (GGA-PBE) has become the most popular approximation due to its balance between computational efficiency and accuracy.[88] Unfortunately, both LDA and GGA suffer self-interaction errors from inadequate cancellation of self-Coulomb and self-exchange energies, impacting the effectiveness of predicted material properties like electron band structures.

In addressing the above limitations of LDA and GGA, additional computational methods, such as hybrid functionals,

Table 1. Brief descriptions, advantages, and disadvantages of approximations to the exchange–correlation functional and vdW models in FPC applied to the InAs-based vdW research.

	Methods	Descriptions	Advantages	Disadvantages	Refs.
Approximations to the Exchange–correlation Functional	LDA	The exchange–correlation energy at each spatial point only depends on the electron density at that point.	Suitable for homogeneous electron gas systems.	Self-interaction error.	[79]
	GGA	The exchange–correlation energy depends on the electron density and the electron density gradient.	Better correctness than LDA in systems with inhomogeneous electron densities.	Self-interaction error.	[79]
	Meta-GGA	The exchange–correlation energy depends on the electron density, the electron density gradient, and the kinetic energy density gradient.	Higher accuracy in systems with strong electron correlation.	Self-interaction error.	[79]
	Hybrid functionals	It partially incorporates Fock exchange with semi-local exchange–correlation energy from DFT.	Accurately predict band structures in various systems.	High computational resources and costs are needed.	[80]
	GW approximations	G is the Green's function, and W is the screened Coulomb interaction.	Effective in predicting the crystal structures and electronic properties of semiconductor materials.	High computational resources and costs are needed.	[80]
	Hubbard U correction	It integrates cost-effective Hubbard-like models into LDA or GGA.	Adept at handling systems with strong electronic correlations.	Difficult to accurately determine Hubbard U parameters.	[81]
VdW Models	DFT-D2	It describes vdW interactions with fixed C_6 coefficients independent of the molecular environment.	Good precision in layered structure systems.	Higher empiricism than DFT-D3.	[82]
	DFT-D3	It describes vdW interactions with refined C_6 coefficients based on atomic coordination numbers.	Higher accuracy, less empiricism, and broader chemical applicability than DFT-D2.	Higher computational costs than DFT-D2.	[83]
	Tkatchenko-Scheffler	It obtains accurate C_6 coefficients and vdW radii from the ground-state electronic density of molecules or condensed matter.	Not dependent on empirical parameters.	Analytical gradients are not readily available.	[84]

GW approximations, and Hubbard U correction, are introduced. Among them, hybrid functionals stand out for their ability to accurately predict band structures in various systems, achieved by blending a part of Fock exchange with semi-local exchange–correlation energy from DFT. GW approximations effectively predict the crystal structures and electronic properties of semiconductor materials, where G is the Green's function, and W is the screened Coulomb interaction.[80] However, both these methods demand substantial computational resources and bear higher costs. Hubbard U correction achieves a trade-off between these two demands. It is particularly adept at handling systems with strong electronic correlations through integrating cost-effective Hubbard-like models into LDA or GGA.[81]

2.3.3. VdW Models

Several vdW models have been promoted to describe vdW interactions in layered structures. The reliability of these vdW models is highly affected by the accuracy of the C_6 coefficients, which serve as parameters characterizing the intensity of non-covalent interactions between molecules or atoms.[89,90] The semi-empirical DFT-D series methods are currently extensively utilized. Both DFT-D1 and DFT-D2 utilize fixed C_6 coefficients that remain unaffected by the molecular environment.[82,91] In contrast, DFT-D3 attains higher accuracy, less empiricism, and broader chemical applicability by fine-tuning the C_6 coefficients using empirical geometric factors derived from atomic coordination numbers.[83,92] The Tkatchenko–Scheffler (TS) approach directly derives precise C_6 coefficients and vdW radii from the ground-state electronic density, offering theoretical robustness compared to DFT-D methods.[84] However, it struggles to provide analytical gradients for the exchange-hole dipole moment method.[93,94] For these reasons, the TS approach, as a vdW model, is rarely used to calculate InAs.

The prevalent use of FPC in semiconductor research has spurred the creation of various software and codes. Several leading software and codes in this domain can produce relatively consistent results on major critical issues, with their accuracy comparable to that of high-precision experiment measurements, ensuring the feasibility, reliability, and, therefore, credibility of computational methods.[95,96]

3. VdW Epitaxy of InAs-based Materials

Pure crystalline phase InAs nanostructures and single-atom-layer 2D InAs films are integral foundational elements in fabricating InAs-based vdW heterostructures, opening new avenues for perfect and hybrid vdW integration.[97–100] Although the synthesis of these materials remains unrealized, a plethora of research efforts are dedicated to pushing the leap forward in this regard. This section focuses on InAs-based materials grown by vdW epitaxy, mainly encompassing InAs NWs, NW heterostructures, QDs, and InAs films, whose morphological features and crystal quality are somewhat influenced by the surface states.

3.1. InAs Nanowires

Vertically aligned growth of InAs NWs is advantageous for device fabrication and functional application since directional growth effectively reduces parasitic effects and non-ideal factors caused by unwanted cross-junctions between separate NWs.[101] Therefore, discussions concerning well-aligned InAs NWs grown by vdW epitaxy are necessary. This part involves nucleation and growth, process optimization, and crystal-phase engineering of InAs NWs.

3.1.1. Nucleation and Growth

Since the first successful growth of InAs NWs on graphite (GR) surfaces by CF-MOVPE,[102] research results on vdW epitaxial growth of InAs NWs are heavily reported, among which the understanding of the growth of InAs NWs on GR or GN substrates is relatively in-depth. Several factors are found affecting the nucleation and growth of these NWs. The first one is the obtuse contact angle at the vdW heterogeneous interfaces between InAs NWs and GR films, as shown in **Figure 4a**. From an energetic standpoint, it initiates the formation of the lateral facets and the subsequent axial growth of InAs NWs.[102] The second one is the surface steps that provide preferential nucleation sites for InAs NWs, such as ledges and kinks. The ledges and kinks form surface potential wells, which increase the residential time of the precursor around the surface steps and thus improve the nucleation probability of InAs NWs.[102] The third one is the defects states. The growth direction and number density of InAs NWs correlate with GN's surface roughness. Although moderately rough surfaces benefit the nucleation density of InAs NWs, highly rough surfaces deteriorate the vertical growth mode of InAs NWs by impeding the effective formation of vdW interfaces.[103]

The heteroepitaxial relationship between InAs NWs and substrates also affects the growth orientation of InAs NWs. The most important relationship is considered to be the one named coherent heteroepitaxy, which refers to a generalized lattice matching, i.e., the aligned arrangement of coincident in-plane lattices. On the one hand, it benefits the vertical growth of InAs NWs. Hexagonal prismatic InAs NWs vertically grow along the $[\bar{1}\bar{1}\bar{1}]$ direction on GN (0001), as demonstrated in Figure 4b when there exists the nearly coherent heteroepitaxial relationship of InAs $(\bar{1}\bar{1}\bar{1})[\bar{1}10]||GN(0001)[1\bar{2}10]$.[103] On the other hand, it influences the sidewall growth of InAs NWs. InAs NWs exhibit modulated growth from the core segment $\{2\bar{1}\bar{1}\}$ to the shell segment $\{1\bar{1}0\}$ on the center of the MoS_2 micro-plate, as depicted in Figure 4c. This primarily stems from the relative lack of nucleation sites on the vdW surfaces, which causes preferential nucleation on the low adsorption energy sites on interior facets.[104] In brief, obtuse contact angle, surface steps, defect states, and heteroepitaxial relationship collectively influence the nucleation and growth of InAs NWs in the initial growth stages.

3.1.2. Process Optimization

Extensive experiments have explored a variety of principles and approaches of process optimization aimed at improving the geometric structures and increasing the number density of InAs NWs, as detailed in **Table 2**. These process optimization strategies can be categorized into three primary technical directions:

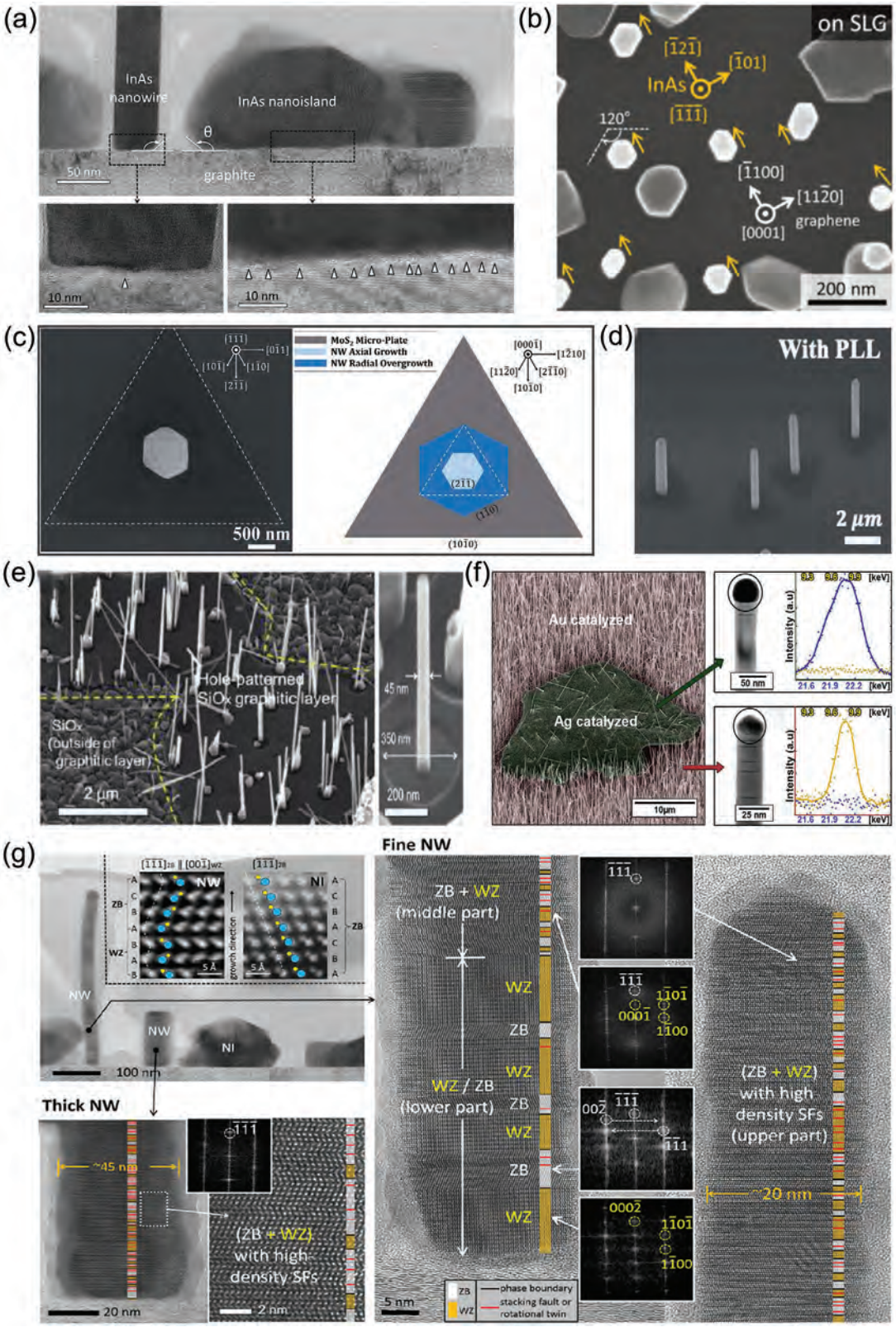

Figure 4. VdW epitaxial InAs NWs. a) Obtuse contact angle appearing at heterogeneous interfaces between InAs NWs, InAs nanoislands, and graphite films. Reproduced with permission.[102] Copyright 2011, ACS. b) Nearly coherent heteroepitaxial relationship between InAs NWs and graphene films. Reproduced with permission.[103] Copyright 2012, ACS. c) Lattice alignment and in-plane orientation relationships between InAs NW core segment, InAs NW shell segment, and triangular MoS_2 microplate. Reproduced with permission.[104] Copyright 2021, Royal Society of Chemistry (RSC). d)

optimal growth parameter windows, pre-growth surface treatments, and selective-area growth (SAG).

First, the prevailing approach is to explore the optimal growth parameter windows. One routine practice is to adjust growth conditions, such as growth time, temperature, V/III flux ratio, etc. This practice hardly yields consistent and comparable quantitative results due to the distinct growth parameter windows for varying growth mechanisms and equipment machines. However, it can achieve InAs NWs with maximal aspect ratio and number density while ensuring InAs nanoislands with minimal area coverage. Another refined method is the two-step flow-modulated growth (TFMG), where high number density nucleation sites of InAs NWs are formed at the initial low trimethylindium (TMIn) flow rate stage, and the axial growth of InAs NWs is created in the subsequent high TMIn flow rate stage. This method ensures a comparable number density of InAs NWs without sacrificing the aspect ratio.[105]

Second, pre-growth surface treatments are a much simpler approach than optimal growth parameter windows. In the case of GN substrates, by eliminating the conventional arsine (AsH_3) surface treatment, the aspect ratio and number density of InAs NWs are significantly increased, accompanied by a decrease in the area coverage of InAs nanoislands.[105] InAs NWs developed in such growth mode bear a striking resemblance in number density and aspect ratio to those formed under optimal V/III flux ratios. This is attributed to the enhanced surface migration of the growth species and the reduced formation of parasitic islands when no AsH_3 surface treatment is applied. In the case of MoS_2 substrates, pre-growth poly-L-lysine (PLL) surface treatment promotes the formation of single InAs NW on individual, isolated, triangular MoS_2 domains while suppressing parasitic growth along MoS_2 edges and surfaces, as this growth mode reduces the surface roughness of MoS_2 surfaces and allows for charge compensation of dangling bonds on MoS_2 edges, as shown in Figure 4d.[104] Therefore, pre-growth surface treatments achieve a high aspect ratio in InAs NWs and suppress discrete parasitic islands that differ from the continuous polycrystalline InAs films.

Thirdly, SAG is a scalable method for designing and controlling the density, position, diameter, and pattern of InAs NW arrays.[106] One type of SAG is mask-assisted growth, in which the mask layers cover the naturally formed step-edges of the GR films to suppress parasitic growth. Thus, InAs NWs are selectively grown on the hole-patterned GR films, shown in Figure 4e.[102] The second type of SAG is metal-catalyzed-assisted growth. Au catalysts are favored for growing InAs NWs on InAs substrates, while Ag catalysts are preferred for growing InAs NWs on GR substrates. The difference in the selectivity of InAs NWs to the metal catalysts is attributed to the longer diffusion length of Au on GR substrates than that of Au on InAs substrates, which can inhibit the growth of Au-seeded NWs on GR substrates, shown in Figure 4f.[107]

In short, exploring the optimal growth parameter windows is beneficial to realize InAs NWs with high aspect ratio and number density. Pre-growth surface treatments effectively suppress the undesirable discrete parasitic growth of InAs nanoislands. Moreover, SAG contributes significantly to fabricating large-scale, periodically aligned InAs NW arrays.

3.1.3. Crystal-Phase Engineering

InAs NWs grown by vdW epitaxy generally demonstrate intricate crystal-phase mixing and transitioning rather than an ideal pure crystalline state. From the bottom to the top, these NWs evolve into three parts: an alternating ZB or WZ (WZ/ZB) lower part, a mixed WZ and ZB (WZ+ZB) middle part, and a WZ+ZB upper part accompanied by SFs, as evidenced in Figure 4g.[48] Such polytypic structures pose challenges for the design and fabrication of high-performance devices. To effectively engineer the crystal phase and overcome its drawbacks, researchers explore the underlying formation mechanisms driving such processes and identify the main factors into three aspects: surface energy, interfacial atomic arrangement, and interlayer interactions. The lower surface energy of the WZ phase results in its dominance over the ZB phase during the initial growth stage of InAs NWs.[108] The interfacial atomic arrangement also affects the crystal phase at the initial growth stage. Specifically, InAs WZ (0001)A exhibits greater stability than InAs ZB (111)A as the smaller lattice mismatch between InAs WZ and GN enables the alleviation of heterogeneous interface stress. As the growth progresses, InAs NWs shift from the initial WZ phase to the subsequent ZB phase due to the enhanced phase stability of ZB in structures exceeding lateral sizes of 10.8–20.1 nm. It should be emphasized that vdW interactions primarily impact only the early growth stage of InAs NWs; their influence diminishes as the InAs overlayer nanostructures extend, giving way to interior ionic lattice layers and internal fields dictating the crystal-phase preference.[48]

3.2. Nanowire Heterostructures

NW heterostructures grown by vdW epitaxy are a special kind of heterostructure, mainly in the form of InAs-based ternary NWs and double heterostructures with InAs NWs on one side of the intermediate substrate layer.

InAs-based ternary NWs exhibit structural diversity from both homogeneous and inhomogeneous NWs. Homogeneous InAsSb NWs developed on GR[114] and homogeneous InGaAs NWs formed on MoS_2[109] are observed. Inhomogeneous structures present different forms caused by distinct processes, ranging from self-organized core–shell configurations to the more complex axial and coaxial NW heterostructures. InGaAs NWs grown on GN display spontaneous core–shell phase segregation under conventional processes in **Figure 5**a. This phenomenon is attributed to the absence of dangling bonds on GN, which prohibits strain sharing between InGaAs and GN.[109] Complementing these empirical observations, theoretical research claims that such self-organized core–shell structures stem from the combination of nucleation barriers and atomic diffusion effects.[68]

InAs NWs poly-L-lysine surface treatment. Reproduced with permission.[104] Copyright 2021, RSC. e) Growth mask-assisted growth. Reproduced with permission.[102] Copyright 2011, ACS. f) Metal-catalyzed-assisted growth. Reproduced with permission.[107] Copyright 2016, IOP Publishing. g) Crystal-phase transition from WZ/ZB to the ZB+WZ mixture of InAs NWs. Reproduced with permission.[48] Copyright 2018, AIP.

Table 2. Growth conditions and morphological characteristics of InAs NWs and NW heterostructures grown by vdW epitaxy.

Material	Substrate	Growth mechanism	Process optimization	Time [min]	Temp [°C][a]	V/III	L [μm][b]	D [nm][c]	Density [$\times 10^8$ cm^{-2}]	Refs.
InAs NWs	SLG[d]	CF-MOCVD[e]		10	550	20 ± 1	3.40 ± 0.15	87.00 ± 17	7.00	[109]
	SLG	CF-MOCVD	AsH_3+TFMG	5	650	25	4.20	51.70	8.30	[105]
	h-BN	CF-MOCVD		15	500	10	0.98	50.33	21.00	[110]
	SLG	CF-MOVPE		20	560			20.00		[48]
	SLG	CF-MOVPE		20	560			40.00 ± 14	1.60 ± 0.7	[103]
	MLG[f]	CF-MOVPE		20	560				6.90 ± 1.1	[103]
	GR[g]	CF-MOVPE	SAG	20	560		0.80 ± 0.40	42.00 ± 16	6.00	[102]
	GR	Au-MOVPE		5	450					[111]
	GR	SC-MBE[h]		20	450–500		0.82 ± 0.28	78.00 ± 5	4.00	[112]
	GR	SC-MBE		60	450	55	3.00		0.255	[113]
	GR	SC-MBE		60	435	55	2.58 ± 0.34	31.21 ± 6.59	8.09	[108]
	GR	SC-MBE		60	420–500		2.58 ± 0.34	31.20 ± 6.60	8.09	[114]
	GR	Ag-MBE	SAG	15	417	15	10.00	20-50		[107]
	MoS_2	SC-MOCVD	PLL	10	700	25	2.35	430.00		[104]
InAsSb NWs	GR	SC-MBE		120	420–500		4.70 ± 0.89	46.00 ± 6.9	1.46	[114]
InGaAs NWs	MoS_2	CF-MOCVD		10	570	20 ± 1	5.00	75–520		[109]
InAs/InGaAs coaxial NWs	SLG	CF-MOCVD		10	570	20 ± 1	2.00	132 ± 24		[109]
InAs/InGaAs axial NWs	MLG ($n = 4$)	CF-MOCVD	TFMG	10	550–570		2.11 ± 0.35	89.00 ± 22		[115]
InAs/InGaAs coaxial NRs	MLG ($n = 10$)	CF-MBE	TFMG	60	380		10.00	110.00	5.00	[116]
InAs NWs/SLG/InAs NWs	SLG	CF-MOVPE		20	560		1.03 ± 0.46	63.00 ± 10	1.90 ± 0.9	[117]
							0.29 ± 0.12	41.00 ± 7	2.50 ± 1.6	
InAs NRs/MLG/ZnO NTs	MLG ($n = 10$)	CF-MBE		35	450		3.00	50.00	5.00	[118]

[a] Temp: Temperature; [b] L: Length; [c] D: Diameter; [d] SLG: Single-layer graphene; [e] CF: Catalyst-free; [f] MLG: Multi-layer graphene; [g] GR: Graphite; [h] SC: self-catalyzed.

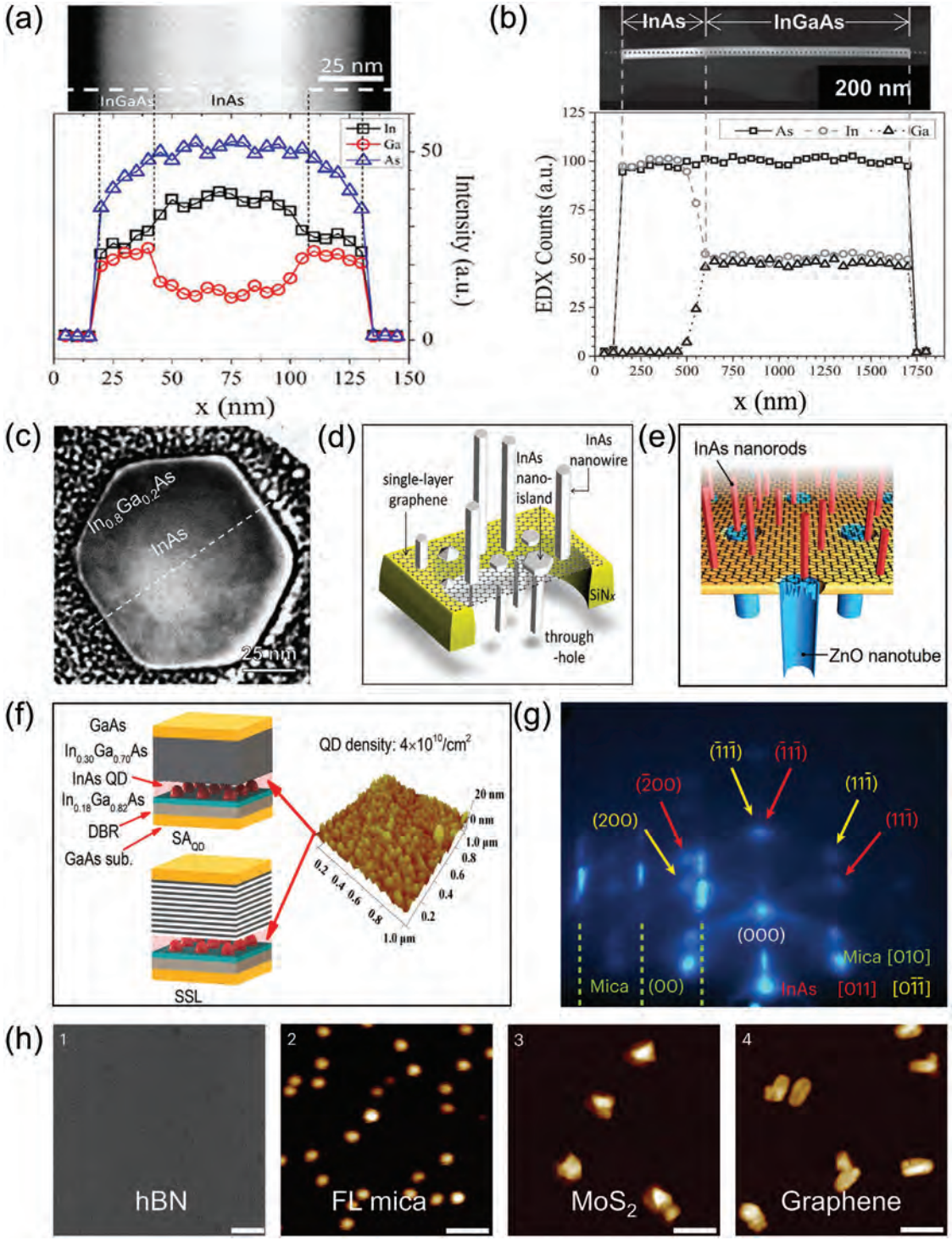

Figure 5. a–e) VdW epitaxial InAs NW heterostructures. a) Self-organized core–shell heterostructured InAs/InGaAs NWs. Reproduced with permission.[109] Copyright 2013, ACS. b) Axially heterostructured InAs/InGaAs NWs. Reproduced with permission.[115] Copyright 2014, Wiley-VCH. c) Coaxially heterostructured InAs/InGaAs NRs. Reproduced with permission.[116] Copyright 2015, Springer Nature. d) InAs NWs/SLG/InAs NWs double heterostructures. Reproduced with permission.[117] Copyright 2013, Wiley-VCH. e) InAs NRs/MLG/ZnO NTs hybrid heterostructures. Reproduced with permission.[118] Copyright 2021, Springer Nature. f–h) VdW epitaxial InAs QDs. f) InAs QDs covered with capping layers integrated into GN/GaAs vdW heterostructures. Reproduced with permission.[119] Copyright 2020, Springer Nature. g) Non-coherent vdW epitaxial relationship between InAs QDs and FL mica. h) InAs QDs grown on 2D vdW layered materials, including h-BN, FL mica, MoS_2, and GN. Reproduced with permission.[120] Copyright 2024, Springer Nature.

The two-step growth mode is an innovative adaptation to conventional processes, which offers flexibility in manipulating both the geometric structures and chemical composition of NW heterostructures. In one case of two-step growth mode, InAs NWs are initially grown on the GN surface and subsequently covered with InGaAs NWs above the InAs bottom end, forming axial InAs/InGaAs NW heterostructures as exemplified in Figure 5b.[115] In another case of two-step growth mode, ultrafine InAs nanorods (NRs) are first synthesized at high temperature and followed by InGaAs shell layers coated on InAs core layer at low temperature, creating coaxial InAs/InGaAs NR heterostructures, as shown in Figure 5c.[116]

In addition to InAs-based ternary NWs discussed above, double heterostructures with InAs NWs positioned on one side of the intermediate substrate layer emerge as another unique form of NW heterostructures. Examples of these configurations are the InAs NWs/single-layer GN (SLG)/InAs NWs[117] and the InAs NRs/multi-layer GN (MLG)/ZnO nanotubes (NTs),[118] as demonstrated in Figures 5d,e, respectively. The double heterostructures have three major advantages as follows. First, these structures enable efficient vdW integration of disparate materials, as the material growth processes on both sides of the intermediate substrate layer are mutually independent. Second, each material can maintain its intrinsic electronic and optical properties without interference from adjacent materials. Finally, these structures can flexibly integrate the unique characteristics of different materials to design complex and multi-functional InAs-based vdW devices, which is difficult to achieve in conventional single-material systems.

Research on these InAs-based ternary NWs and double heterostructures represent innovative explorations in materials science. Leveraging precise control over their chemical composition and geometric structures, these distinctive InAs NW heterostructures offer new possibilities for designing innovative InAs-based vdW devices, thereby expanding the range of applications.

3.3. InAs QDs

Recent advances in the vdW epitaxial growth of InAs QDs have attracted increased interest, although they remain relatively rare. Earlier research documented the integration of InAs QDs into GN/gallium arsenide (GaAs) vdW heterostructures as common substrates, as depicted in Figure 5f.[119] The integrated structures combine the high carrier transport efficiency of vdW heterostructures and strong light–matter interactions of InAs QDs. Precisely, the vdW heterostructures function to tune the band gap of GN, thereby boosting photon harvesting and carrier transfer across the interfaces. The InAs QDs aid the radiative recombination process of photo-generated carriers, which are covered by several capping layers rather than direct contact with the 2D layered materials. Further research claimed that laser annealing can significantly improve the interfacial quality of these heterostructures, thereby enhancing their optical and electronic properties.[121]

The latest research achieved direct vdW epitaxial growth of InAs QDs on various 2D layered materials, such as h-BN, fluorophlogopite (FL) mica, MoS_2, and GN, as appeared in Figures 5g,h.[120] The intrinsic vdW interactions and optimal growth parameter windows foster efficient atomic collisions at the vdW interfaces, where atoms can freely diffuse across due to the low surface energy and absence of dangling bonds of 2D vdW materials. Such atomic collisions are pivotal in the seeding process for QD formation. Additionally, the density of InAs QDs on FL mica is highly sensitive to temperature, varying mainly from 1.6×10^{11} to 2.5×10^{7} cm^{-2} with just a tiny shift from 200 to 340 °C.

3.4. InAs Films

Research targeting the vdW epitaxial growth of InAs films is relatively less than NWs. There are two main modes for vdW epitaxial growth of InAs ultrathin films, as detailed in **Table** 3. The first one is the Stranski–Krastanov growth mode, where the gradual expansion of clusters or nanoislands forms continuous ultrathin films. With this mode, lateral expansion of nanoislands into horizontal InAs ultrathin films is observed after the growth of NWs is inhibited on h-BN, as shown in **Figure** 6a.[110] These InAs ultrathin films predominantly exhibit ZB and WZ/twin structures with crystal defects, as depicted in Figure 6b. Such mixed crystalline phase of InAs ultrathin films is similar to InAs NWs.

The second one is the layer-by-layer growth mode. With this mode, triangular InAs ultrathin films are grown on mica. The atomically flat mica surfaces with no dangling bonds facilitate the diffusion and accumulation of InAs molecules, resulting in InAs layered structures.[122] The thickness of the triangular InAs ultrathin film is ≈4.8 nm, and the thinnest sublayer InAs is 0.35 nm, matching the subunit cell thickness of InAs along the [0001] direction, as shown in Figure 6c. It implies a layer-by-layer growth mode in forming the nonlayered 2D InAs. InAs ultrathin films grown on mica exhibit higher crystal quality with no apparent defects than those grown on h-BN, as evidenced by the atomic sites with perfect periodicity in Figure 6d. The relatively few research studies reveal serious challenges associated with vdW epitaxial growth of InAs ultrathin films, among which the most rewarding one is the synthesis of single-atom-layer InAs films in experiments.

Thicker InAs films are widely used as substrate materials, some of which can form vdW heterostructures with other vdW materials. As evidence, weak vdW interactions with a vdW gap of 3.5 Å between the semimetal $ZrTe_2$ films and the InAs (111) 2×2 substrates are observed, despite the presence of apparent lattice mismatch (≈6.6%) in Figure 6e.[123] Besides, weak vdW interactions exist between Ge–Sb–Te (GST) films and InAs (111) reconstructed surfaces under the case of a lattice mismatch of ≈1%. InAs (111)A 2×2 reconstruction (A1) and InAs (111) B 2×2 reconstruction (B1) surfaces are found more favorable for vdW integration than other reconstruction forms, as shown in Figure 6f.[124] These results highlight that InAs-based materials are crucial in vdW-integrated systems. However, the successful synthesis of desirable monolayer and few-layer InAs vdW films is currently impossible in experiments.

3.5. Layer Transfer Methods

Given the challenges in directly synthesizing pure InAs-based vdW structures, layer transfer techniques are essential for achieving heterogeneous and mixed-dimensional vdW integration of

Table 3. Growth conditions and morphological characteristics of InAs films grown by vdW epitaxy.

Material	Substrate	Growth mechanism	Time [min]	Temp [°C][a)]	Precursor condition	Morphological characteristics	Refs.
InAs flakes	mica	CVD	0.5–22	770–850	InAs powder	thickness down to 4.8 nm, lateral sizes up to ≈37 µm	[122]
InAs films	h-BN	CF-MOCVD	30	475	V/III = 200	NA[b)]	[110]

[a)] Temp: Temperature; [b)] NA: not available.

InAs NWs or films with other materials. Methods for transferring 2D materials are diverse.[125–128] However, the strong covalent bonds of InAs limit the current use of only the following three techniques, as summarized in **Table 4**.

The first method, mechanical exfoliation, uses adhesive tape to detach materials from epitaxial substrates and transfer them onto target substrates, achieving InAs/WSe_2 vdW heterostructures with low-density interfacial traps.[129] Although straightforward, this method struggles with precise control of thickness, shape, and position, which is essential for accurate layer alignment and lattice arrangement. Introducing carriers such as polymethylmethacrylate (PMMA) and polydimethylsiloxane (PDMS) increases controllability and predictability.

The second method involves PMMA support. In this approach, PMMA-coated InAs layers are transferred to target substrates after removing sacrificial layers.[130,131] The high mechanical strength of PMMA ensures the integrity and flatness of InAs layers, allowing precise transfer and positioning. However, this method is more cumbersome than mechanical exfoliation due to

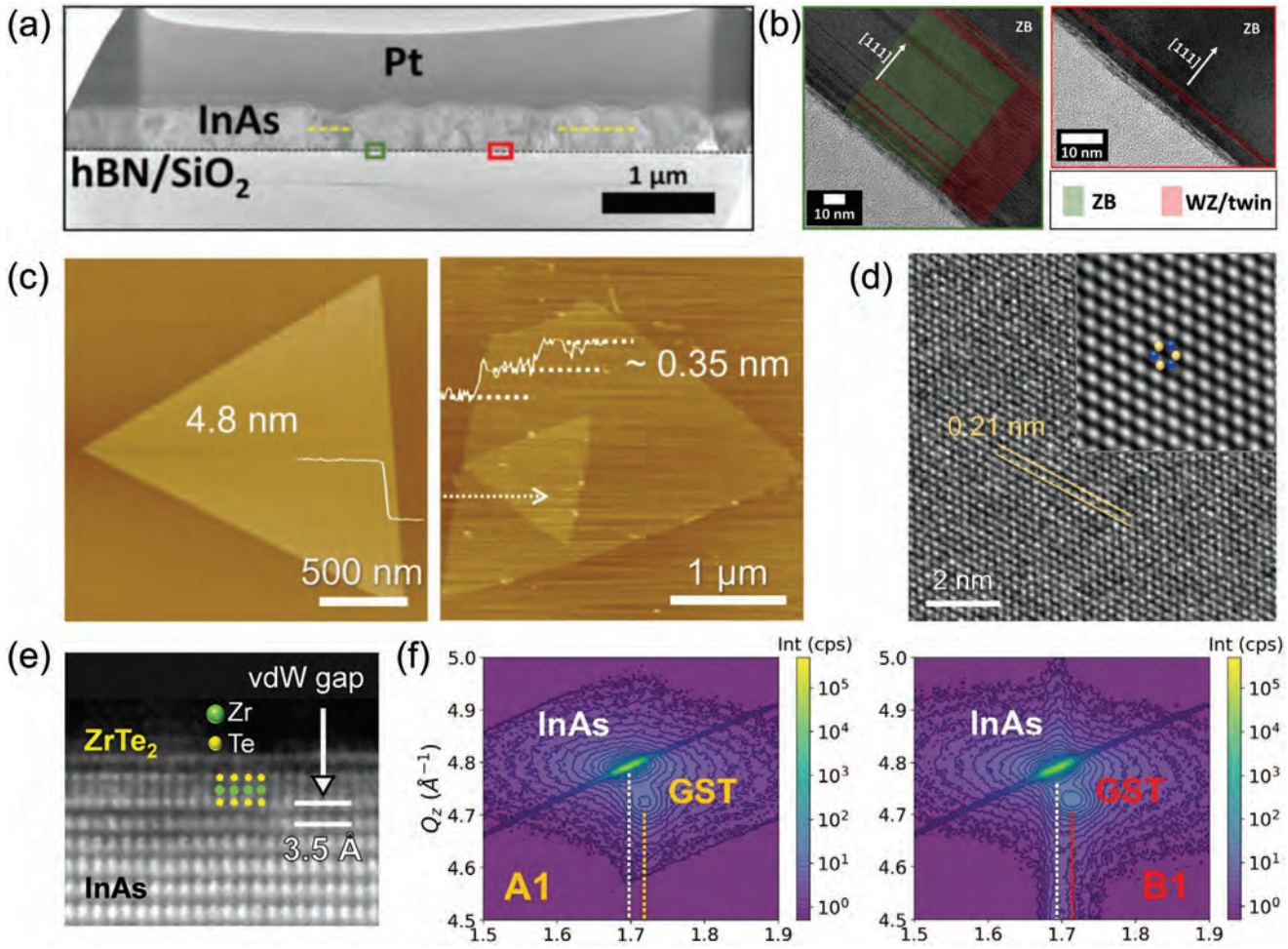

Figure 6. a–d) VdW epitaxial InAs ultrathin films. a) InAs ultrathin films grown on h-BN by Stranski–Krastanov mode. b) Polycrystalline InAs with ZB and WZ/twin defects. Reproduced with permission.[110] Copyright 2023, IOP Publishing. c) InAs ultrathin films grown on mica in layer-by-layer mode. d) High crystalline quality InAs without distinct defects. Reproduced with permission.[122] Copyright 2022, Springer Nature. e, f) VdW epitaxy using thicker InAs films as substrates. e) $ZrTe_2$ films grown on InAs (111) 2 × 2 substrates with lattice mismatch ≈6.6%. Reproduced with permission.[123] Copyright 2018, ACS. f) GST alloys grown on InAs (111)A 2 × 2 reconstruction (A1) and InAs (111) B 2 × 2 reconstruction (B1) surfaces with lattice mismatch ≈1%. Reproduced with permission.[124] Copyright 2022, Wiley-VCH.

Table 4. Comparison among three predominant layer transfer methods for InAs-based materials.

Methods	Transferred materials	Carriers	Advantages	Disadvantages	Refs.
Mechanical exfoliation	InAs quantum membranes	Adhesive tape	Straightforward.	Low precision.	[129]
PMMA supporting	InAs (ultrathin) films	PMMA	More precise positioning than mechanical exfoliation. Preserve the integrity and flatness of films.	More cumbersome than mechanical exfoliation. Unable to completely remove polymer holders.	[130,131]
PDMS exfoliation	(patterned) In(Ga)As layers or In(Ga)As-based building blocks	PDMS	Faster transfer speed and cleaner heterogeneous interfaces than PMMA supporting.	Induce interfacial wrinkles and stresses.	[133–137]

multiple steps and potential polymer contamination at vdW interfaces.

The third method, PDMS exfoliation, is preferred for constructing InAs vdW heterostructures.[132] It uses PDMS to separate and transfer In(Ga)As layers or In(Ga)As-based blocks from donor substrates to target materials after selective wet etching of sacrificial layers. This method has successfully created InAs/GN,[133,134] In(Ga)As/Si,[135,136] and InGaAs/InP/GaN[137] vdW integrated structures. The distinct advantage of PDMS exfoliation is its transfer printing mechanism, which enables conformal contact and flat vdW interfaces, providing faster transfer speeds and cleaner heterogeneous interfaces compared to PMMA requiring polymer removal. Badly, the softness of PDMS can induce minor wrinkles and stresses in InAs films.

Future advancements aim to improve purity, sustainability, and automation. Innovative techniques, such as ice-stamp transfers[138] and machine-learning-based automatic identification and stacking,[139] are expected to surpass traditional limitations.

4. VdW Integration of InAs-based Devices

Various InAs-based vdW heterojunction devices have been successfully prepared using the vdW integration technique in experiments, covering diodes, transistors, solar cells, photodetectors, and devices integrated with Si. The key performances of these devices are summarized in **Figure 7**. This section focuses on discussing and analyzing the key role of the vdW heterojunctions on the performance of these devices. These works highlight the broad prospect of the InAs-based vdW heterojunctions in device applications and build a substantial foundation for the further exploration and advancement of InAs-based vdW research.

4.1. Diodes

The performance of InAs-based vdW heterojunction diodes is predominantly influenced by interfacial charge transfer and the generated built-in electric field. The built-in electric field across vdW heterojunctions can effectively separate electrons and holes, reducing carrier recombination and enhancing diodes' rectifying characteristics. It is reported that both the InAs/WSe_2 and InAs/InSe vdW heterojunction diodes exhibit rectifying behavior because of the interfacial charge transfer process, as shown in **Figures 8a,b**.[129,140] Their structural difference lies in the position of the InAs layers. Layer transferred InAs membrane is stacked on top of mechanically exfoliated WSe_2 vdW membrane in the InAs/WSe_2 structure. In contrast, the InAs/InSe structure is formed by peeling off and transferring the InSe vdW flake upon the InAs epilayer. Among these two vdW structures, the I_{ds}–V_{ds} output characteristics of the InAs/WSe_2 diode closely match those of an ideal diode, and a higher rectification ratio is achieved for this diode. This near-ideal electrical properties benefit from its cleaner vdW heterojunction interface, in which defects or impurities can cause issues such as increased leakage current and decreased conductivity.

The built-in electric field generated in the process of interfacial charge transfer also contributes to the optical detection capabilities of these diodes. For instance, the InAs/InSe vdW heterojunction photodiode displays a broadband optical response that ranges from NIR to VIS bands with responsivity exceeding 0.2 A W^{-1} at 633 nm and 0.02 A W^{-1} at 984 nm, owing to the unique optical properties of the InAs-based vdW heterojunctions, as shown in Figure 8c.[140] Specifically, with the assistance of the built-in electric field, the photogenerated electrons and holes in InAs-based vdW heterojunction devices are quickly separated and collected by the external circuit with low recombination probability and high optical responsivity.

4.2. Transistors

High-quality InAs films have high electron mobility, which is beneficial for enhancing the electron transport efficiency of InAs-based vdW heterojunctions.[130,131] Such an enhancement is crucial for their widespread application in high-performance and low-power electronic devices. The vertical field-effect transistor (FET) based on InAs/GN vdW heterojunction where InAs film is exfoliated with PDMS and dry transferred on top of GN attains output current density up to 45 000 A cm^{-2}, surpassing that of GN/MoS_2/metal vertical FETs.[133] This impressive output characteristic benefits from the excellent electron transport capability of the InAs/GN vdW structure, where the highly conductive InAs channel layer overcomes the limitations associated with the poor vertical transport capability of 2D layered materials and minimizes the series resistance of the GN electrodes. An additional factor contributing to this achievement is the implementation of the self-aligned metal contacts where GN is used as the drain electrode and top metal is grounded as the source, which results in

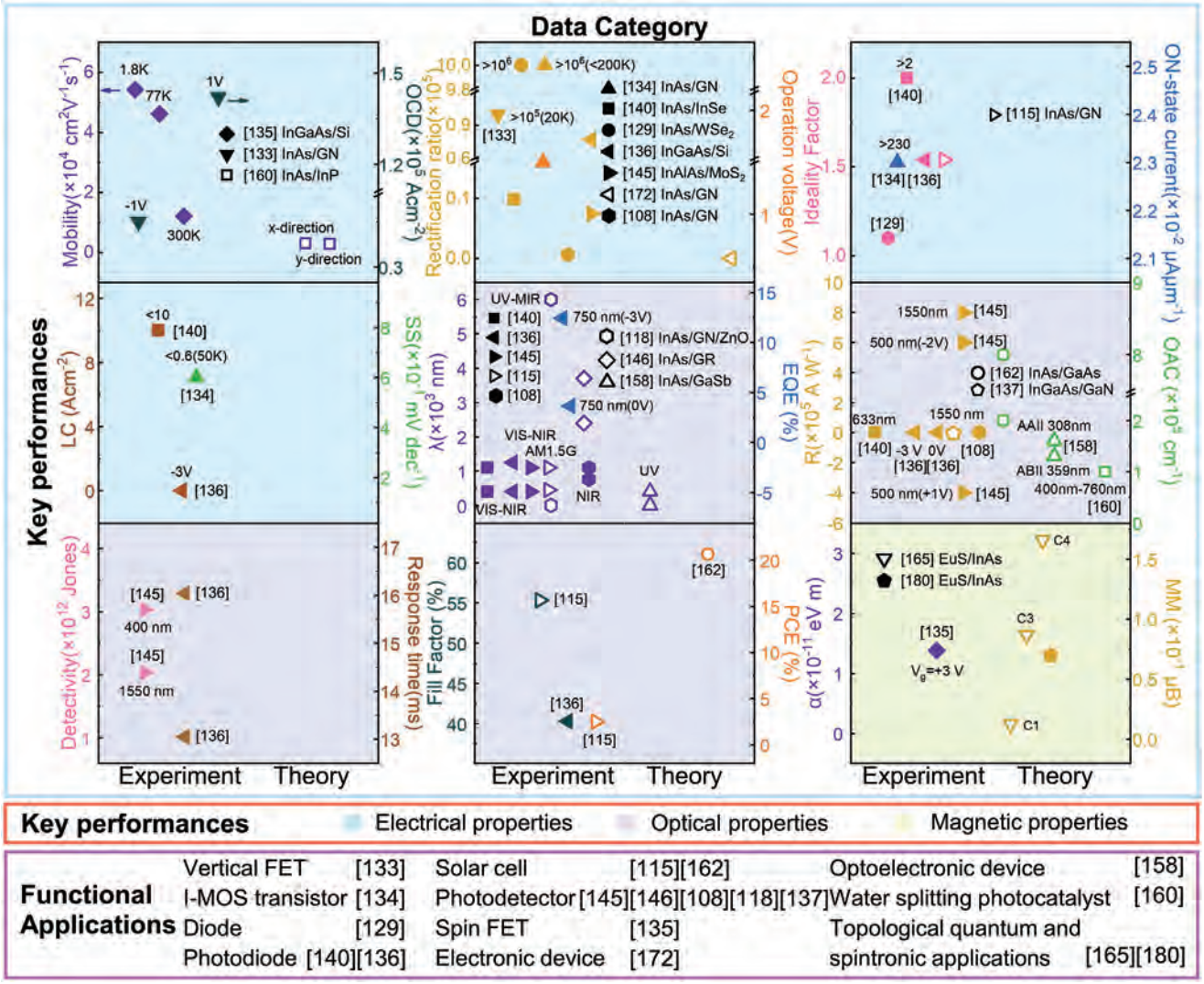

Figure 7. Key performances and functional applications of diverse InAs-based vdW devices summarized from both experimental and theoretical research discussed in Section IV and Section V. a)GN: Graphene; b)OCD: Output current density; c)LC: Leakage current; d)SS: Subthreshold swing; e)λ: Wavelength; f)EQE: External quantum efficiency; g)UV: Ultraviolet; h)MIR: Mid-infrared; i)VIS: Visible; j)NIR: Near-infrared; k)GR: Graphite; l)R: Responsivity; m)OAC: Optical absorption coefficient; n)PCE: Power conversion efficiency; o)α: Rashba SOI parameter; p)MM: Magnetic moment.

more linear rectifying behavior of the vertical FET, as illustrated in Figures 8d–f. This rectifying behavior with the p-type Schottky barrier further signifies a noticeable effect of Fermi-level pinning within the InAs/GN vdW structure. This differs from the behavior observed in GN/transition metal dichalcogenides vertical FETs.[133]

The high-conductance channel InAs film is also PDMS exfoliated and vdW-bonded upon GN in impact ionization metal oxide semiconductor (I-MOS) transistor based on InAs/GN vdW heterojunction. GN is biased as a drain, and InAs is grounded as a source in this I-MOS transistor configuration, which differs from the previously discussed self-aligned FET. The I-MOS transistor achieves a remarkable on-state current of 230 μA μm^{-1}, owing to the lateral electron transport capability of the InAs/GN vdW structure. It also offers an operation voltage of 1.5 V lower than the Si-based devices and an SS of less than 0.6 mV Dec^{-1} driven by efficient gate control for high-speed switching, as depicted in Figures 8g–i.[134] These findings indicate that the excellent electron transport capability of InAs-based vdW materials can facilitate the design and fabrication of innovative, high-performance vdW transistors.

4.3. Solar Cells

The InAs NW heterostructures grown by direct vdW epitaxy demonstrate remarkable efficiency in harvesting photogenerated carriers. Three different groups of NW heterostructures with InAs NWs as the bottom end are shown in Figure 8j, ranging from A to C.[115] In addition to preventing self-organization phase segregation of InGaAs NWs as previously discussed, the InAs bottom end grown on GN acts as both low series resistance

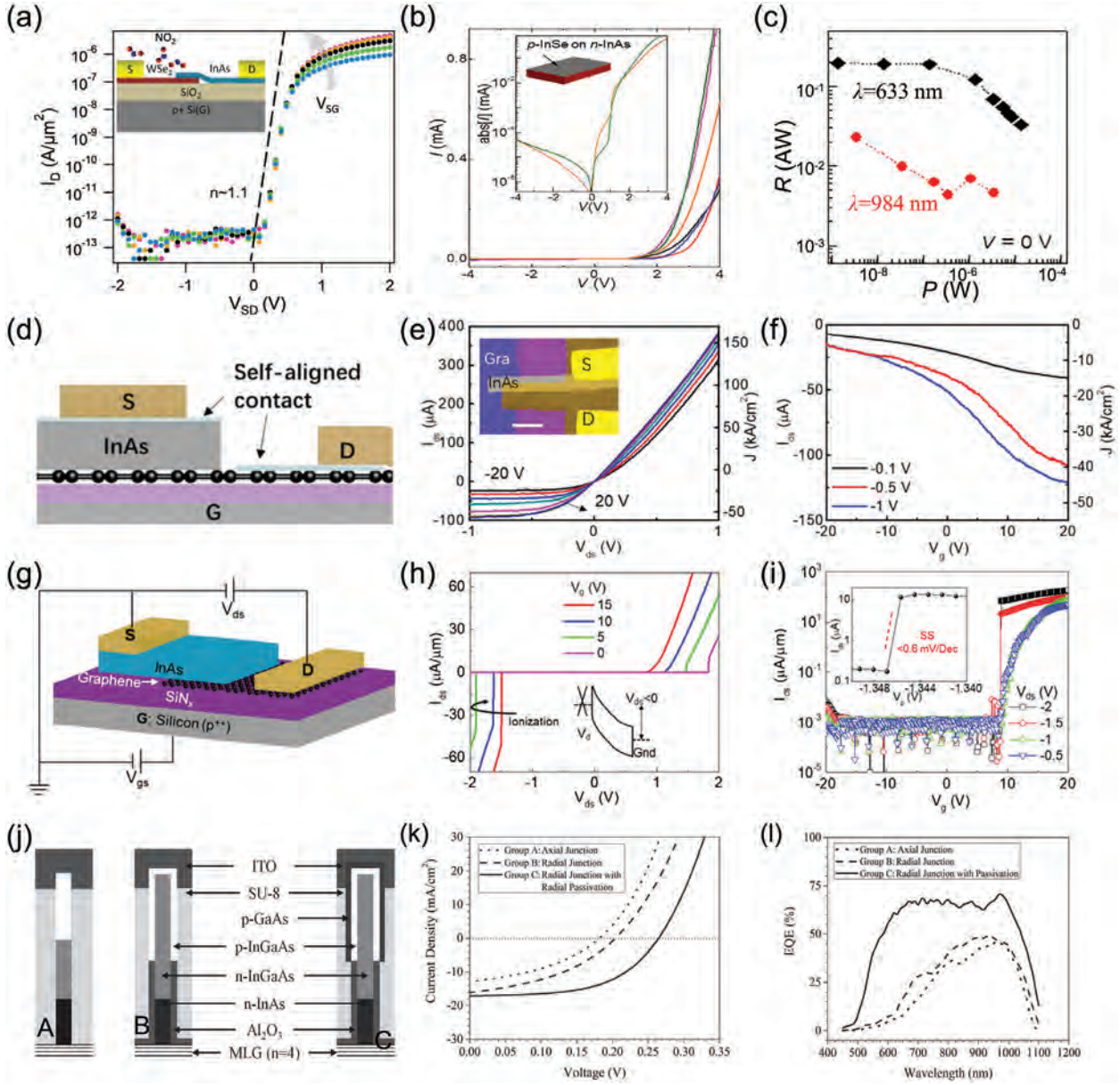

Figure 8. a) I_{ds}–V_{ds} output characteristics of the near-ideal InAs/WSe_2 vdW heterojunction diode with clean vdW heterogeneous interface. Reproduced with permission.[129] Copyright 2013, AIP. b) *I*–*V* characteristics and c) Responsivity at 633 and 984 nm of the highly-mismatched InAs/InSe vdW heterojunction photodiode. Reproduced with permission.[140] Copyright 2016, AIP. d–f) Self-aligned vertical FET based on InAs/GN vdW heterojunction. d) Schematic of device structure with InAs film transferred and vdW integrated on GN. e) I_{ds}–V_{ds} output characteristics demonstrating rectifying behavior, and the p-type Schottky barrier is attributed to the fermi level pinning effect within the InAs/GN vdW structure. f) I_{ds}–V_g transfer characteristics showing a high output current density of 45 000 A cm^{-2} due to the excellent electron transport of the InAs/GN vdW structure. Reproduced with permission.[133] Copyright 2019, ACS. g–i) I-MOS transistor based on InAs/GN vdW heterojunction. g) Schematic of device structure by vdW integrating transferred InAs film with GN. h) Low operation voltage of 1.5 V appeared in I_{ds}–V_{ds} output characteristics, and i) small steep SS < 0.6 mV Dec^{-1} appeared in I_{ds}–V_g transfer characteristics attributing to efficient gate control of InAs/GN vdW structure at 50 K. Reproduced with permission.[134] Copyright 2021, Wiley-VCH. j) Schematic of solar cells based on the axial junction (Group A), radial junction (Group B), and radial junction with radial passivation (Group C) of InAs/InGaAs NW arrays grown on GN by direct vdW epitaxy. k) *J*–*V* characteristics and l) EQE of solar cells based on InAs/InGaAs NW arrays, ranging from group A to C. Reproduced with permission.[115] Copyright 2014, Wiley-VCH.

point contacts and electron collection layers. Within these groups, group A contains axial p–n junctions within the InGaAs segments, group B integrates radial p–n junctions, and group C introduces in situ growth of p-type GaAs shell segments for surface passivation building upon group B.

Among them, solar cells based on group C of InAs/InGaAs NW arrays demonstrate the best photovoltaic performance with an open-circuit voltage (V_{oc}) of 0.26 V, a short-circuit current density (J_{sc}) of 17.16 mA cm^{-2}, an EQE of 71%, a fill factor (FF) of 55.32%, and a PCE of 2.51%. It is a new record for solar cells

based on III-V NWs with embedded junctions grown on GN, as shown in Figures 8k,l.[115] These exceptional photovoltaic properties directly arise from the InAs NW heterostructures grown by direct vdW epitaxy. The secondary cause for the excellent photovoltaic properties lies in the innovative design of the device architectures. Specifically, the InAs bottom end collects photogenerated electrons, and the GaAs passivation layer prevents the recombination of electron–hole pairs induced by photons absorbed from the higher energy spectral range. Together, the InAs NW heterostructures and strategic device architectures boost electron collection efficiency and mitigate electron–hole recombination, thereby significantly improving the photovoltaic performance of solar cells.

4.4. Photodetectors

As shown in the pioneering work by Hu et al.,[141] asymmetrically localized fields formed with heterogeneous integration will boost performance[142] and infrared photodetectors' spectral-dimension functionality.[77] This idea was subsequently confirmed by many excellent works, especially those utilizing vdW materials that do not require lattice matching.[143,144] VdW heterostructures with various InAs-based materials demonstrate remarkable optoelectronic performance in photodetectors. For InAs-based films (**Figure 9a**), the MoS_2/InAlAs/InGaAs n–i–n vdW photodetector by integrating the MoS_2 sheet onto the recessing-exposed InAlAs barrier layer enables dual-band detection, where the MoS_2 layer is sensitive to the VIS band and the InGaAs layer can detect the NIR band.[145] In the case of VIS illumination, the responsivity can be modulated from 6×10^5 to -4×10^5 A W^{-1} by manipulating the MoS_2 gate field, as illustrated in Figure 9b. In the case of NIR illumination, the photodetector exhibits a high responsivity exceeding 8×10^5 A W^{-1}, owing to the internal photocurrent amplification in the InGaAs channel layer. The transferred charges across MoS_2/InAlAs vdW heterojunction interfaces lead to a detectivity (D*) of 3×10^{12} cmHz$^{1/2}$W^{-1} at 400 nm and 2×10^{12} cmHz$^{1/2}$W^{-1} at 1550 nm, which are on par with traditional photodetectors based on Si, Ge, and InGaAs, as shown in Figure 9c.[145]

For single InAs NW (Figure 9d), the NIR InAs/GN vdW photodetector with InAs NW physically transferred onto GN achieves a responsivity of 0.5 A W^{-1} and an I_{light}/I_{dark} of 5×10^2, which are greater than GN photodetectors and single InAs NW due to the enhanced optical capabilities imparted by the InAs-based vdW heterojunctions, as depicted in Figures 9e,f.[146] The near-field enhancement effect is an important technique for new detectors to improve their sensitivity.[147] On the one hand, sophisticated artificial optical structure design is often required to achieve a high absorption rate in bulk material. On the other hand, even if the absorption rate tends to be unitary in bulk materials, it is usually challenging to obtain high quantum efficiency because the absorption region is separated from the position of the built-in electric field. It is only in recent years that there have been individual efforts[148] to achieve extreme quantum efficiency by introducing a transverse transmission mode that allows the built-in electric field to coincide with the enhanced region of the optical field. Furthermore, for InAs NW arrays (Figure 9g), the InAs/GR IR vdW photodetector prepared by directly vdW epitaxial growth of InAs NWs on GR exhibits rectifying characteristics and a cutoff wavelength of 3.4 μm at room temperature with the primary peak at ≈2.7 μm, indicating optical capability within the NIR and MIR bands, shown in Figures 9h,i.[108] VdW photodetectors based on InAs NW arrays possess better optical characteristics than those based on single InAs NW because larger surface areas can realize a total absorption of incident light.[149]

For InAs NW heterostructures, Figure 9j shows the dual-band photodetector based on directly epitaxial InAs/MLG/ZnO vdW heterostructure, as detailed in Section 3.2.[118] The Au-InAs-MLG on the one side of this double heterostructure exhibits nonlinear *I–V* characteristics, similar to typical two-terminal devices with Schottky contacts on both terminals, as shown in Figure 9k. Photocurrent generation commences on this side when photon energy reaches 0.5 eV and peaks ≈0.6 eV, corresponding to the MIR band, as shown in Figure 9l. The Au-ZnO-MLG on the other side of this double heterostructure demonstrates photocurrent generation within the UV band. In addition, photogating is also one of the essential technologies for improving detector performance, especially for low-dimensional structures such as NWs with huge surface-to-volume ratios. The core–shell structure with a photogating effect can significantly suppress the dark current of InAs NWs to reduce device noise,[150] and improve device response, and even obtain single-photon response at room temperature.[151] Typically, the novel localized characterization techniques, such as spatially resolved photocurrent mapping, confined-carriers-sensitive scanning probe microscopy, and minority-carriers-sensitive scanning probe microscopy, have been pioneeringly established,[9,142] offering a profound avenue for unveiling interesting non-equilibrium phenomena in HgCdTe,[152,153] unique trap-related p–n junction transformation in HgCdTe,[154] and abnormal local defect states in InAs NWs[150] thereby constituting a pivotal factor in propelling photodetector development. For example, Hu et al. pioneered the development of high-performance infrared photodetectors with positive/negative responses based on InAs NWs[150] and single-photon photodetectors based on CdS NWs.[151]

Thus, InAs vdW heterojunction photodetectors with InAs films, InAs NWs, and InAs NW heterostructures demonstrate outstanding optoelectronic performance. These skillfully integrated structures using InAs vdW materials realize multifunctional photodetectors on a single chip while the unique properties of each material are fully exploited. This innovative integration strategy significantly boosts the responsivity and broadens the detectable spectral range of InAs-based vdW photodetectors.

4.5. Integration with Bulk Materials

The vdW integration of InAs-based materials with bulk covalently bonded materials has significantly advanced InAs vdW technology, enabling the development of traditional semiconductor integrated systems for multi-functional applications.[155,156] The transfer process and resulting structure fabricated by selective wet-etching and contact printing are shown in **Figure 10a**.[135] InAs HEMT is vdW-bonded on top of SiO_2/Si substrate. The electron mobility of the transferred InAs HEMT is ≈54 200 cm^{2}V^{-1}s^{-1} at 1.8 K and 12 100 cm^{2}V^{-1}s^{-1} at 300 K,

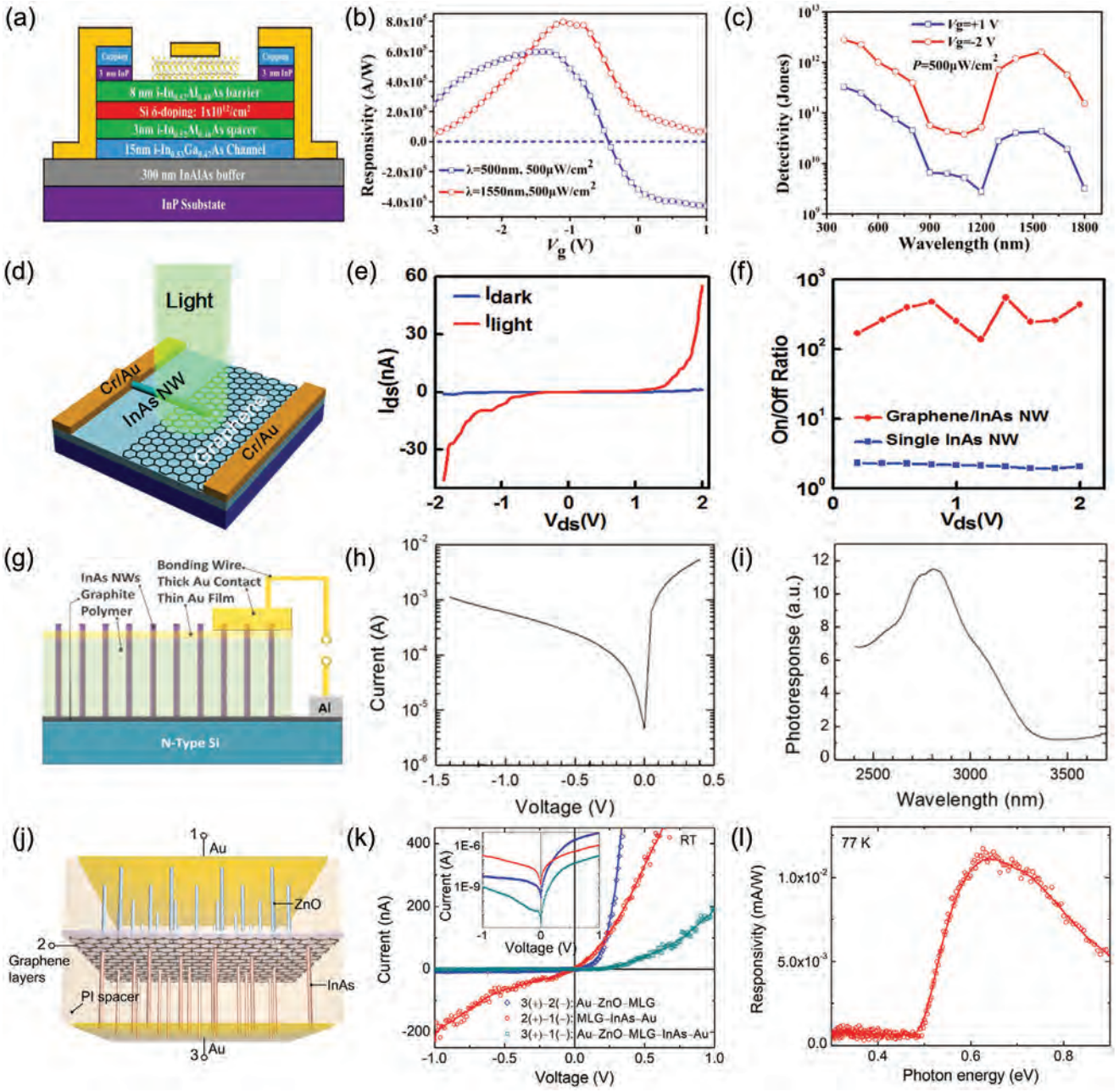

Figure 9. a–c) Dual-band MoS_2/InAlAs/InGaAs vdW heterojunction photodetector. a) Schematic of the device structure fabricated by integrating MoS_2 sheet with HEMT based on InGaAs/InAlAs heterojunction. b) High responsivity measured at 500 and 1550 nm illumination under 500 μW cm^{-2}. c) Detectivity of 3×10^{12} Jones at 400 nm and 2×10^{12} Jones at 1550 nm. Reproduced with permission.[145] Copyright 2019, Wiley-VCH. d–f) InAs/GN vdW heterojunction NIR photodetector. d) Schematic of the device structure with InAs NW physically transferred onto GN. e) I_{ds}–V_{ds} output characteristics and f) on/off ratio of 5×10^2 under incident laser wavelength of 1 μm. Reproduced with permission.[146] Copyright 2015, Wiley-VCH. g–i) InAs/GR vdW heterojunction IR photodetector. g) Schematic of the device structure by direct vdW epitaxial growth. h) *I*–*V* characteristics and i) photoresponse measured at room temperature. Reproduced with permission.[108] Copyright 2017, Springer Nature. j–l) Dual-band InAs NRs/MLG/ZnO NTs vdW heterojunction photodetector. j) Schematic of the device structure by direct vdW epitaxial growth. k) *I*–*V* characteristics measured at room temperature and l) photoresponse of the Au-InAs-MLG measured at 77 K. Reproduced with permission.[118] Copyright 2021, Springer Nature.

surpassing that of the III-V compound semiconductor-based HEMTs integrated onto Si substrates, as shown in Figure 10b.[135] Its Rashba SOI parameter (α) highly depends on the gate electric field. This has been interpreted as a result of interfacial vdW interaction and strain relaxation in the InAs channel layers, as shown in Figure 10c. SOI refers to the intricate coupling between the spin and orbital motion of microscopic particles (e.g., electrons),[157] by which the modulation of the electronic structures and magnetic properties of InAs-based materials becomes feasible.[15,38]

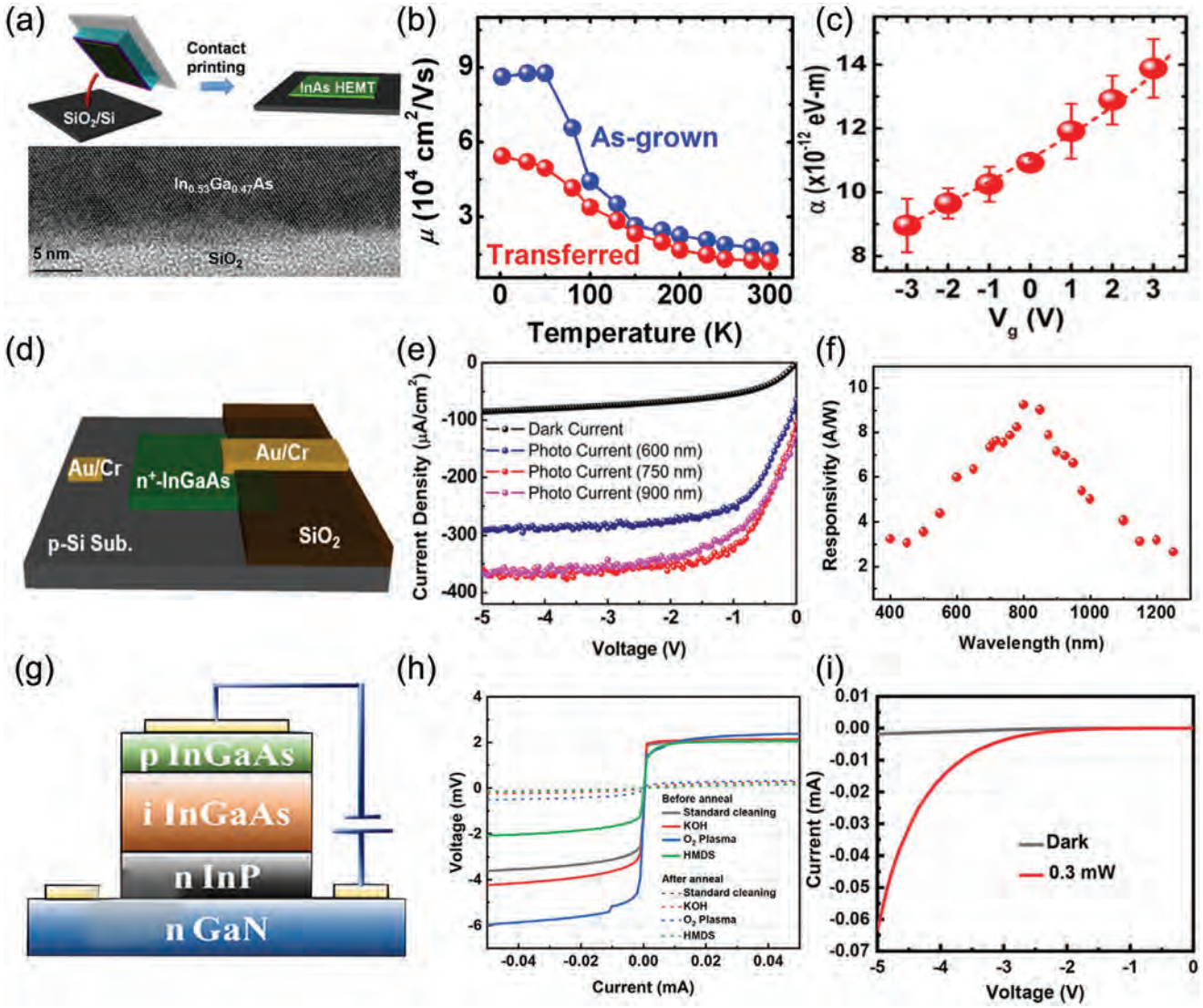

Figure 10. a–c) Spin FET with InAs HEMT vdW integrated onto SiO_2/Si substrate. a) The contact printing process and resulting InGaAs/SiO_2 vdW-bonded interface. b) Electron mobility of 54 200 $cm^2V^{-1}s^{-1}$ at 1.8 K and 12 100 $cm^2V^{-1}s^{-1}$ at 300 K for as-grown and transferred InAs HEMT. c) Gate-controlled Rashba SOI parameter (α) in transferred InAs HEMT. Reproduced with permission.[135] Copyright 2013, ACS. d–f) InGaAs/Si vdW heterojunction photodiode. d) Schematic of a device structure with InGaAs nanomembrane vdW-bonded on Si substrate through transfer printing. e) High photoresponse characteristics at 600, 750, and 900 nm. f) High responsivity over 2.6 A W^{-1} in the broad wavelength range from 400 to 1250 nm under reverse bias of −3 V. Reproduced with permission.[136] Copyright 2016, ACS. g–i) vdW integrated InGaAs/GaN photodetector. g) Schematic of device structure with InGaAs-based p–i–n membranes vdW-bonded on GaN through micro-transfer printing. h) Quasi-linear *IV* characteristics of the InP/GaN vdW structure under different surface treatments after annealing. i) High photoresponsivity of 0.5 A W^{-1} measured at 1550 nm illumination under 0.3 mW. Reproduced with permission.[137] Copyright 2024, ACS.

InGaAs/Si vdW heterojunction photodiode prepared by the epitaxial layer transfer printing of InGaAs nanomembrane onto Si substrate exhibits an impressive photodetection capability, as shown in Figure 10d. The fundamental reason behind this is that this vdW structure reduces the dark current through a clean vdW-bonded InGaAs/Si interface while at the same time enhancing the photocurrent from the benefit of high carrier mobility within the InGaAs layer, as shown in Figure 10e.[136] Its responsivity is greater than 2.6 A W^{-1} in the broadband spectral range from 400 to 1250 nm, which conventional Si photodetectors can otherwise achieve, as shown in Figure 10f.[136] The broad spectral response is ascribed to the distinct sensitivity of constituent materials to varying optical response bands. Moreover, the optical response range can be extended, and the optical absorption capabilities can be enhanced by tuning the material layers' thickness or doping concentration.

The latest vdW heterogeneous integrated InGaAs/GaN photodetector in Figure 10g also demonstrates excellent optoelectronic properties.[137] The p-InGaAs/i-InGaAs/n-InP stacks serve as the core for photo-detecting, with the InP and GaN vdW-bonded together by micro-transfer printing. Various surface treatments optimize the interfacial contact between InP and

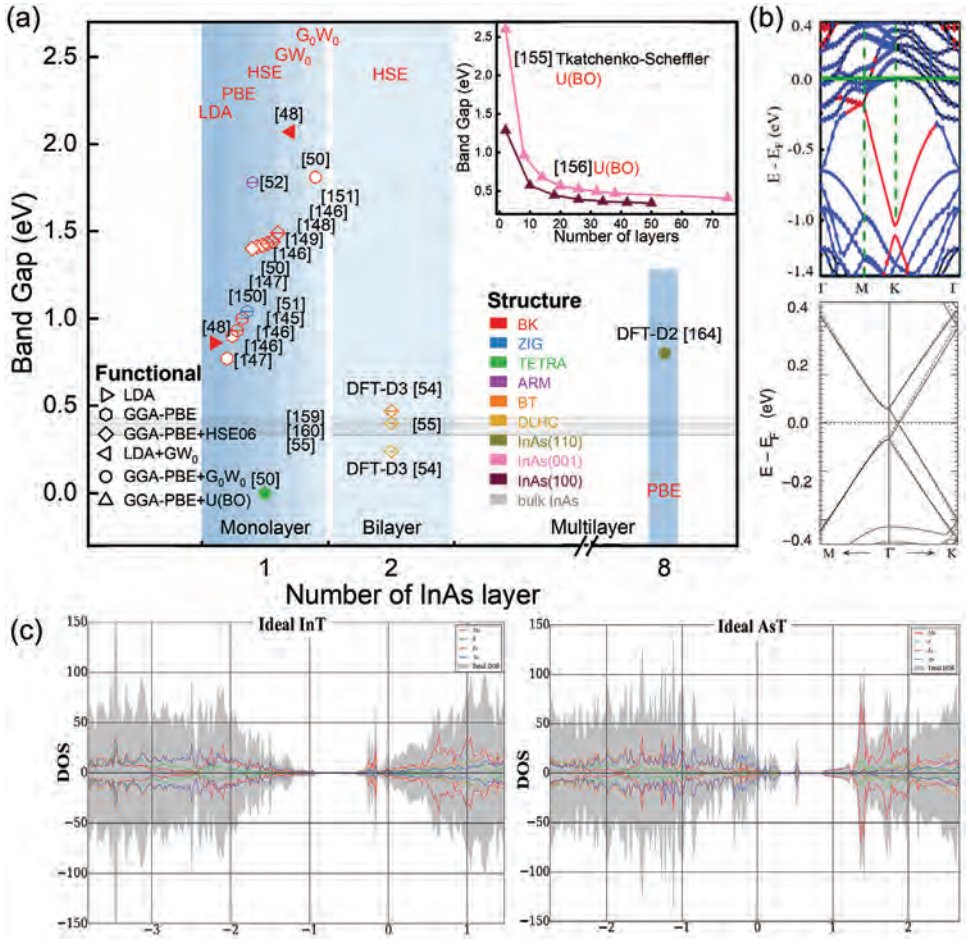

Figure 11. a) Band gap sizes are a function of the number of layers for various InAs structures predicted by different computational methods summarized from the literature. b) Band gap opening for GN layers in InAs/GN vdW heterostructures induced by the interfacial charge transfer. Reproduced with permission.[167] Copyright 2017, RSC. Reproduced with permission.[174] Copyright 2011, APS. c) Electron orbital hybridization for MoS_2/InAs vdW heterostructures is caused by the transfer of electrons in outer orbitals to empty states. Reproduced with permission.[168] Copyright 2021, Elsevier.

GaN, thus enhancing this vdW structure's IV characteristics under reverse bias, as depicted in Figure 10h. The device achieves a remarkable responsivity of 0.5 A W^{-1} when excited at a wavelength of 1550 nm, as illustrated in Figure 10i. This exceptional performance can be attributed to the efficient photogenerated carrier harvesting in the InGaAs absorption layer and the effective vdW bonding between the covalently bonded semiconductor interfaces of InP and GaN. The successful vdW integration is primarily attributed to their microtransfer printing technique and the atomically smooth surfaces across interfaces after a comprehensive array of surface treatments.

In brief, the In(Ga)As nanomembranes or blocks are successfully integrated with other bulk materials through vdW force, which validates the feasibility of the technical route of vdW integration. This presents a beneficial approach to achieving more prosperous function and paves the way for the advancement and application of vdW materials within traditional semiconductor domains.

5. First-Principles Calculations of InAs-Based VdW Systems

This section concentrates on representative research findings related to InAs-based vdW topics from extensive research achievements of FPC. Energetically stable InAs-based vdW materials and stackings and the interfacial charge transfer characteristics across heterojunctions are summarized. The intrinsic relationship between the interfacial charge transfer process and the physical properties of these vdW materials and heterojunctions are then emphasized.

5.1. Energetically Stable Heterostructures

A comprehensive examination of the electronic band structures of InAs is imperative before investigating the energetically stable vdW heterostructures. The characteristic band gaps of InAs extracted from electronic band structures are summarized from the literature in **Figure** 11a. For monolayer, BK InAs, basic DFT tends

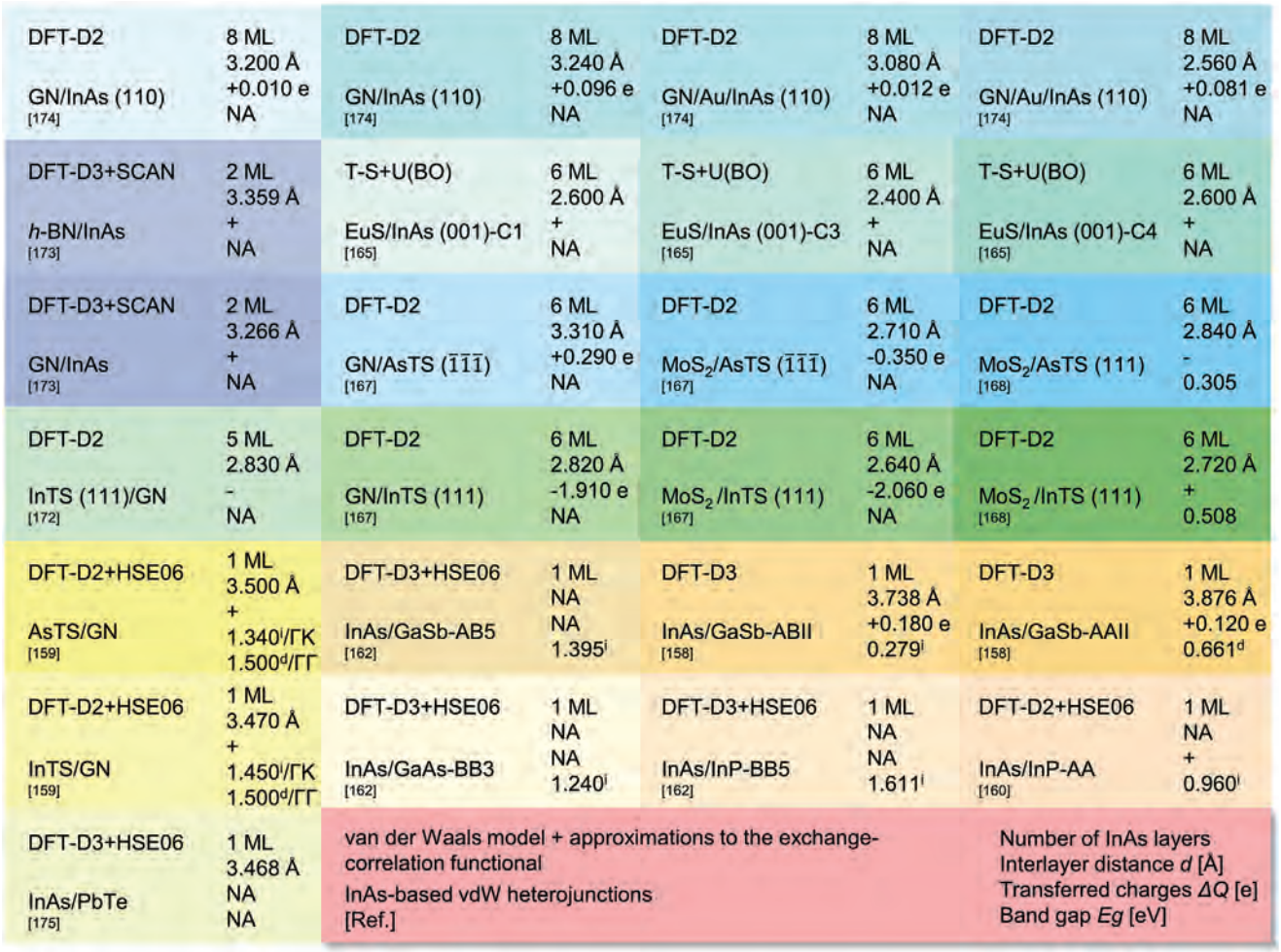

Figure 12. Energetically stable InAs-based vdW heterostructures screened out by reported FPC. The red panel highlighted in the lower right corner illustrates the meaning of the various parts of each panel. In each panel, computational methods are displayed in the upper left corner, while structural parameters and electronic properties are listed on the right-hand side. GGA-PBE is omitted when denoting computational methods because it is used in all cases here. [a] NA: not available; [b] GN: Graphene; [c] SCAN: Strongly constrained and appropriately normed; [d] U (BO): Hubbard U parameter by Bayesian optimization; [e] AsTS: As-terminated InAs surface; [f] InTS: In-terminated InAs surface; [g] The plus sign indicates charge transfer from 2D layered materials to InAs, while the minus sign is the opposite; [h] The upper labels *i* and *d* indicate the indirect and direct bandgap, respectively.

to slightly underestimate band gap sizes,[49,158–160] while GW calculations often overestimate them.[49,51] Hybrid functionals like Heyd–Scuseria–Ernzerhof (HSE06) can correct errors in both methods.[51,159–164] The calculated band gap types for monolayer BK InAs depend on the computational methods used,[51,158–164] reflecting the complexity and uncertainty of the electronic structures. Positively, various computational methods consistently yield nearly identical lattice constants of ≈0.43 nm.[51,159–162] Multi-layer InAs, such as sheets or slabs, exhibit layer-dependent band gap sizes,[165,166] enriching integrated devices' structural design and innovation based on few-layered InAs. Additionally, theoretical calculations extract more critical parameters from electronic band structures, such as effective mass, mobility, and work function.[160,162,164,167–170] However, these parameters receive relatively less attention, as they have gone too far beyond available experimental verifications.

Vertical vdW heterostructures combining InAs with heterogeneous 2D layers offer new platforms for multi-functional devices. They require careful evaluation of vdW interactions with adjacent layers. FPC aims to assess the energy stability of InAs-based vdW heterostructures, evaluating system energy through total[171] or derivative energies such as cohesive,[162] binding,[158,160,167,172,173] adsorption,[174] and formation[168] energies. The minimum total energy indicates stable stacking configurations' equilibrium or quasi-equilibrium states. By this criterion, quite a few energetically stable InAs-based vdW heterostructures have been screened out. They are layer stackings of InAs/GN,[159,164,167,172–174] InAs/GaAs,[162] InAs/GaSb,[158,162] InAs/InP,[160,162] InAs/PbTe,[175] GN/Au/InAs,[174] MoS_2/InAs,[167,168] h-BN/InAs,[173] and EuS/InAs.[165] The structural parameters and electronic properties of these vdW structures and the corresponding computational methods are presented in **Figure 12**. Besides, calculations confirm that variables such as stacking configuration, interlayer spacing, crystal orientation, lattice constant, and surface polarity substantially influence system energy.[158,162,165,167,168] Additionally, In and

As vacancy defects at heterojunction interfaces, coupled with heat exchange, affect the energy stability of InAs-based vdW systems.[168]

To date, single-atomic-layer 2D InAs films have not been successfully synthesized. Thus, achieving ideal InAs-based vdW heterogeneous structures remains impossible. Despite this, researchers remain optimistic as the calculated formation energies of single-layer BK InAs and double-layer DLHC InAs are comparable to existing film materials.[176,177] Continued theoretical efforts to support experimental exploration of InAs vdW monolayers are valuable, as they are essential building blocks for high-performance vdW integrated InAs-based systems.

5.2. Interfacial Charge Transfer Characteristics

FPC is particularly important in assessing the characteristics of interfacial charge transfer caused by the deformation of electronic band structures due to interlayer vdW interactions. They directly affect the size and type of the band gap in InAs vdW heterostructures. For example, band gap opening of GN layers occurs in InAs/GN vdW heterostructures, as shown in Figure 11b, providing a feasible method to tune the semiconductor properties of GN.[167,174] Similarly, in EuS/InAs vdW heterostructures, dispersed states appearing at the valence band maximum of InAs absent in the separated material primarily result from charge transfer to the InAs interfacial layer.[165]

Furthermore, calculations reveal that the band gaps of InAs-based vdW heterostructures depend more on the hybridization of electron orbitals between adjacent interface atoms than on the constituent films themselves, as demonstrated by MoS_2/InAs vdW heterostructures in Figure 11c.[168] This orbital hybridization facilitates the transfer of outer orbital electrons across the interfaces, lowering the system energy to a more stable state. Evidently, interface defects can impart novel features to InAs-based vdW systems by altering vdW force strength and causing changes in interlayer spacing. This alteration directly impacts band structures and the charge transfer process.

VdW forces are susceptible to interlayer spacing fluctuations influenced by lattice orientation, interface configuration, layer thickness, and external stress.[158,162] Accurately quantifying all these factors into a single calculation is complex, leading to significant discrepancies in the band structures of InAs-based vdW systems, even with identical constituent materials. Consequently, the calculated transferred charges across interfaces vary widely or move in opposite directions for similar InAs-based vdW heterostructures.[167,168,172]

5.3. Device Principle and Performance

FPC reveals that charge transfer and built-in electric fields at heterojunction interfaces are crucial for device functionality.[178] This charge redistribution modifies the charge concentration and the conduction type of interfacial atomic layers,[179] potentially transforming InAs films from n- to p-type and altering contact potential barriers with electrode metals (**Figure 13a**).[159,164] InAs-based vdW heterostructures exhibit complex electrical characteristics, including rectifying behavior and negative differential resistance (Figure 13b),[172] all of which are indispensable for junction-type and power devices.

In optoelectronic devices, the built-in electric field from interfacial charge transfer markedly enhances the optical absorption of InAs-based vdW heterostructures beyond their isolated films. MoS_2/InAs vdW structures show higher absorption coefficients from VIS to NIR bands due to stronger vdW interactions and greater charge redistribution than SLG/InAs structures.[167] InAs/GaAs vdW heterojunction solar cells can cover a broad optical absorption range from VIS to IR bands and achieve a power conversion efficiency (PCE) of up to 20.65%, comparable to many excitonic solar cells (Figure 13c).[162] InAs/GaSb vdW heterostructures show higher optical absorption coefficients and a slight blue shift than GaSb and InAs monolayers, enhancing their suitability for UV applications (Figure 13d).[158] These predicted optoelectronic improvements exemplify the photovoltaic potential of InAs-based vdW heterostructures, paving the way for empirical validations and advancements in optoelectronic technologies.

However, despite the superior optical absorption of InAs/InP vdW heterostructures compared to a monolayer, their photocatalytic performance is inferior to GaP/GaAs vdW heterostructures. This is due to the stronger band structure overlap at the interface, which impedes the inhibition of photogenerated carrier recombination.[160] EuS/InAs vdW heterostructures enable spin injection into the InAs layer through proximity-induced magnetism in the spintronic application.[180] Regrettably, the magnetic moment produced is highly localized at the interface, and the strength is too weak to be practical.[165] Therefore, comprehending the material properties and performance limitations of InAs-based vdW heterostructures is crucial for effectively tailoring these materials for multi-functional applications.

Overall, FPC research on InAs-based vdW systems is highly fruitful, highlighting the importance of theoretical calculations amid current experimental dilemmas. FPC predicts the existence of single-atom-layer 2D InAs films, which are not yet fabricated but are urgently needed. These predictions boost experimental researchers' confidence and encourage innovative approaches to overcome existing bottlenecks. Extensive quantitative data on electrical, optical, and magnetic properties will guide advanced vdW system research. This will accurately evaluate InAs-based vdW heterostructure performance and provide reliable prototypes for industrial applications.

6. Summary and Outlook

Significant research advances have been made in InAs-based vdW epitaxial growth technique, the exploration of InAs-based vdW heterogeneously integrated devices, and the quantitative analysis of the physical properties of energetically stable InAs-based vdW heterostructures. The recent achievements and future perspectives in the research of InAs-based vdW materials and devices are visualized in **Figure 14**.

6.1. Epitaxial Growth Techniques

VdW epitaxy effectively fabricates InAs NWs, NW heterostructures, QDs, films, and related materials. NW nucleation and

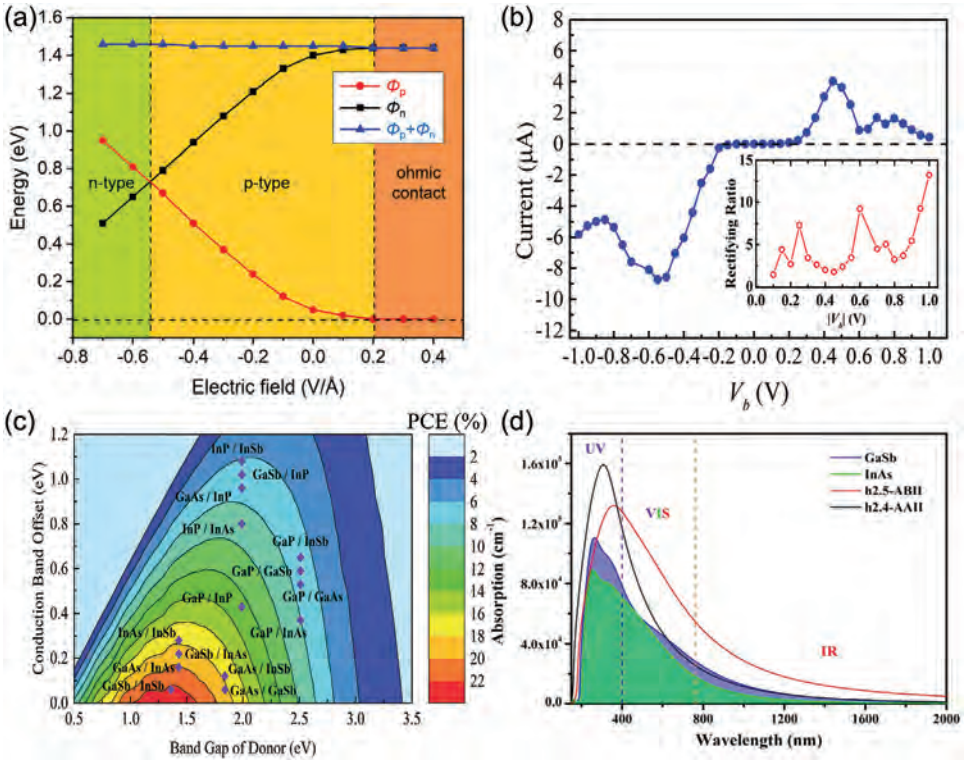

Figure 13. a) Tunable contact type of InAs/GN vdW heterostructures due to interfacial charge transfer process. Reproduced with permission.[159] Copyright 2022, Elsevier. b) Rectifying behavior and negative differential resistance of InAs/GN vdW heterostructures driven by interfacial charge transfer process and vdW interactions. Reproduced with permission.[172] Copyright 2019, Elsevier. c) The PCE of 20.65% achieved in solar cells based on InAs/GaAs vdW heterostructures attributing to enhanced optical capacity. Reproduced with permission.[162] Copyright 2022, Elsevier. d) High UV absorption capacity of InAs/GaSb vdW heterostructures due to charge transfer across vdW heterogeneous interfaces. Reproduced with permission.[158] Copyright 2021, Springer Nature.

growth depend on obtuse contact angle, surface steps, defect states, and heteroepitaxial relationships. Optimization of growth parameters, surface treatments, and SAG achieve high-density and well-aligned InAs NW arrays. InAs NW heterostructures exhibit diverse structural configurations, including axial, radial, core–shell, and double structures. InAs ultrathin films show mixed crystalline phases akin to nanostructures, while thicker films serve as substrates for various vdW heterostructures. These studies advance InAs-based materials for vdW structures and aim to uncover deeper working mechanisms and future development trends.

So far, vdW epitaxy and quasi-vdW epitaxy appear to be the predominant methods for synthesizing InAs-based vdW materials, outperforming traditional InAs growth techniques.[181,182] VdW epitaxial techniques like MBE, MOCVD, and MOVPE enable the creation of high-quality specular interfaces and precise control over atomic-level film thicknesses.[183,184] Conventional CVD rapidly produces large-scale InAs flakes, but the resulting flakes may not strictly qualify as pure vdW materials.[185] Using metal catalysts like Au and Ag in growth enhances InAs NWs and film nucleation on 2D vdW substrates but introduces contaminants and impurity energy levels, shortening minority carrier lifetimes. Consequently, self-catalyzed and catalyst-free growth methods are increasingly favored.[68] Continuously exploring the direct vdW epitaxial growth on 2D layered materials is crucial.[186]

Conventional SAG techniques have been used to fabricate InAs-based vdW materials, offering precise control over nucleation sites on 2D vdW substrates and the lateral diffusion lengths of In adatoms.[106] Building on this foundation, a novel approach known as pinhole-seeded epitaxy is being actively explored.[187,188] This method utilizes pinholes or other openings in layered GN as selective nucleation sites to form continuous films through lateral epitaxy and coalescence processes. Notably, pinhole-seeded epitaxy is, in principle, simplified as these pinholes can occur naturally or be induced during pre-growth annealing without the need for masks.

Current synthesis methods using 1D or 2D substrates have not successfully produced pure crystalline or single-atomic-layer InAs vdW materials. We suggest using 3D curved substrates, such as curved GN or carbon NTs, as alternatives. Recent research with curved 3D substrates has resulted in numerous notable discoveries,[189–194] particularly demonstrating their effectiveness in growing specialized materials like pure crystalline GaAs,[195,196] which is structurally similar to InAs. In principle, curved substrates can facilitate the nucleation and subsequent growth of pure-phase InAs NWs by inhibiting the lateral migration of In adatoms on the smooth surfaces of non-3D substrates. Additionally, the narrow radial space within a curved substrate promotes the aggregation of pure-phase InAs NWs or nanosheets before the onset of the mixed crystal phase, encouraging the formation of 2D geometric stacks bonded by vdW forces. This

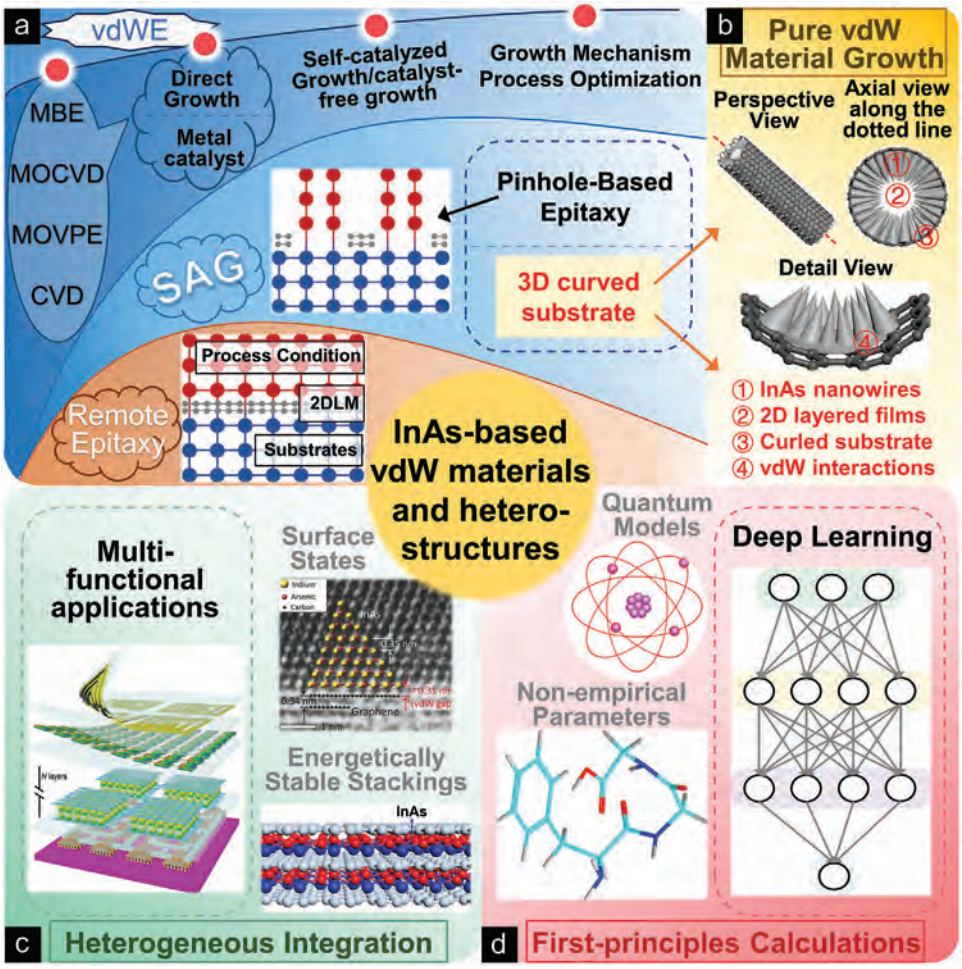

Figure 14. The critical challenges and potential next-generation breakthroughs in the research area of InAs-based vdW materials and heterostructures target four aspects: selective area growth, remote epitaxy, heterogeneous integration, and FPC. a)vdWE: Van der Waals epitaxy; b)2DLM: 2D layered materials.

method selectively directs adatom diffusion and film coalescence during the early stages of InAs vdW growth, thus representing a novel SAG technique. The potential of employing 3D curved substrates warrants further exploration and empirical validation.

The second promising epitaxial technology is remote epitaxy,[197,198] which, while similar to vdW and quasi-vdW epitaxy in the process,[199] differs substantially in growth mechanism. In vdW epitaxy, thin films grow directly on 2D layered substrates, with vdW interactions dictating the structural form and quality of the epitaxial layers. In contrast, remote epitaxy involves depositing new thin films covering a few layers of 2D materials on single-crystal substrates. The properties of the substrates, such as structure and ionicity, primarily influence the crystal structure and quality of the grown films. From a growth mechanism perspective, remote epitaxy expands the scope of vdW growth for single-crystal thin films by relaxing the need for vdW layered substrates. This enhances the diversity of interactions between substrates and epitaxial layers.[200] Given the successful application of this technique to GaAs,[201] InAs, with their similar properties and greater ionicity, hold non-trivial potential for producing superior 2D single-crystal vdW films. Of course, effectively implementing remote epitaxy for InAs 2D materials requires extensive research in three critical areas: selecting appropriate single-crystal substrates, identifying suitable 2D layered cover layers, and refining epitaxial growth processes.

6.2. Integrated Heterostructures and Applications

Although initially an alternative to desirable pure vdW systems, InAs-based vdW heterostructures show great potential in high-performance nanodevices for electronics, optoelectronics, and spintronics. Due to charge transfer and resulting built-in electric fields, vdW diodes can perform rectification and optical detection. The high conductivity of InAs films further improves electron transfer efficiency, enabling high output current and low operating voltage. VdW epitaxial InAs NW heterostructures efficiently harvest photogenerated carriers, enhancing the photovoltaic conversion of solar cells. The diverse compositions of InAs-based vdW heterostructures provide a broad spectral response and high optical absorption. Additionally, integrating InAs with bulk

materials in vdW devices promotes the incorporation of traditional semiconductors into emerging vdW systems.

The primary challenge for InAs-based vdW integrated systems is surface states' diverse and uncertain effects on heterogeneous structures, complicating empirical measurements and performance assessments.[202–204] Advancements in control techniques and accurate theories for stabilizing heterogeneous interfaces are needed. Future research should focus on two key areas: fabricating more energetically stable InAs-based vdW stackings to enhance thermodynamic and chemical stability, including tuning interlayer distances and exploring diverse material combinations to refine electronic and optical properties, and expanding the multi-functional applications of InAs-based vdW devices, as their current range of applications is narrower compared to conventional InAs-based materials. VdW bonding techniques overcome integration limitations from mismatched crystal structures, enabling the integration of diverse materials and leading to more varied InAs-based vdW architectures and applications.

6.3. Theoretical Calculations for VdW Systems

Theoretical calculations have become increasingly valuable due to experimental challenges. FPC identifies various energetically stable InAs-based vdW heterostructures and analyzes the intrinsic relationships between their interfacial charge transfer processes and electronic, optical, and magnetic properties. These findings provide a foundation for scientific research and practical design of InAs-based vdW systems. As theoretical methods advance, FPC will guide experimental programs and innovating mechanisms for InAs-based vdW materials and devices.

However, the accuracy and credibility of FPC for InAs-based vdW systems require refinement. Most approaches rely on semi-empirical DFT-D methods, which need the correction of vital parameters using high-precision experimental data. Unfortunately, such reliable data is currently lacking.[205] Non-empirical vdW models, such as the vdW-DF model, should be explored in future calculations.[171,206–208] The next major challenge is the simplified treatment of InAs-based vdW heterojunction interfaces,[81,165,172] with system energies and crystal structures typically derived at 0 K.[51,168] These issues reduce the reliability of experimental references and necessitate the development of sophisticated quantum models, such as molecular dynamics.[209,210] Unfortunately, this approach requires substantial computational resources, costs, and advanced theoretical frameworks.

The potential solution involves integrating deep learning techniques to enhance FPC for improved computational accuracy, speed, and cost.[211–214] Deep learning uses neural networks with multiple layers to learn abstract data representations.[215–217] With reliable datasets, refined algorithms, and increasing computational power, deep learning has significantly advanced semiconductor materials and devices, aiding in the discovery of stable materials, prediction of physical properties, and acceleration of FPC.[218–220] Deep learning excels at processing extensive, reliable data from FPC, extracting intricate feature relationships, and refining precise mathematical and physical models.[221–225] Integrating deep learning with FPC can greatly expedite material discovery, structural design, and device performance optimization.

In conclusion, the success of scientific research relies on the complementarity of theory and experiment. This is particularly true for studying InAs-based vdW materials and integrated systems. Surprising advancements in these frontier research fields are promising if the experimental and theoretical challenges discussed here are effectively addressed.

Acknowledgements

T.C. and Y.M. contributed equally to this work. The authors are grateful for financial support from the National Natural Science Foundation of China (Grant Nos. 62074085, 62104118, and 62274061).

Conflict of Interest

The authors declare no conflict of interest.

Keywords

2D materials, device, electronic, indium arsenide, van der Waals heterostructure

Received: April 18, 2024
Revised: June 17, 2024
Published online:

[1] A. D. Franklin, *Science* **2015**, *349*, aab2750.
[2] J. A. del Alamo, *Nature* **2011**, *479*, 317.
[3] M. Lundstrom, *Science* **2003**, *299*, 210.
[4] M. Peng, R. Z. Xie, Z. Wang, P. Wang, F. Wang, H. N. Ge, Y. Wang, F. Zhong, P. S. Wu, J. F. Ye, Q. Li, L. L. Zhang, X. Ge, Y. C. Ye, Y. Lei, W. Jiang, Z. G. Hu, F. Wu, X. H. Zhou, J. S. Miao, J. L. Wang, H. Yan, C. X. Shan, J. N. Dai, C. Q. Chen, X. S. Chen, W. Lu, W. D. Hu, *Sci. Adv.* **2021**, *7*, eabf7358.
[5] A. K. Geim, I. V. Grigorieva, *Nature* **2013**, *499*, 419.
[6] Y. Liu, N. O. Weiss, X. Duan, H.-C. Cheng, Y. Huang, X. Duan, *Nat. Rev. Mater.* **2016**, *1*, 16042.
[7] K. S. Novoselov, A. Mishchenko, A. Carvalho, A. H. Castro Neto, *Science* **2016**, *353*, aac9439.
[8] T. He, H. Ma, Z. Wang, Q. Li, S. N. Liu, S. K. Duan, T. F. Xu, J. C. Wang, H. T. Wu, F. Zhong, Y. T. Ye, J. H. Wu, S. Lin, K. Zhang, P. Martyniuk, A. Rogalski, P. Wang, L. Li, H. T. Lin, W. D. Hu, *Nat. Photonics* **2023**, *18*, 60.
[9] F. Wu, Q. Li, P. Wang, H. Xia, Z. Wang, Y. Wang, M. Luo, L. Chen, F. S. Chen, J. S. Miao, X. S. Chen, W. Lu, C. X. Shan, A. Pan, X. Wu, W. C. Ren, D. Jariwala, W. D. Hu, *Nat. Commun.* **2019**, *10*, 4663.
[10] D. Jariwala, T. J. Marks, M. C. Hersam, *Nat. Mater.* **2017**, *16*, 170.
[11] Y. Liu, Y. Huang, X. Duan, *Nature* **2019**, *567*, 323.
[12] T. Li, Y. She, C. Yan, J. Miao, D. Jariwala, *MRS Bull.* **2023**, *48*, 899.
[13] W. Xia, L. Dai, P. Yu, X. Tong, W. Song, G. Zhang, Z. Wang, *Nanoscale* **2017**, *9*, 4324.
[14] X. Zhou, X. Hu, J. Yu, S. Liu, Z. Shu, Q. Zhang, H. Li, Y. Ma, H. Xu, T. Zhai, *Adv. Funct. Mater.* **2018**, *28*, 1706587.
[15] J. F. Sierra, J. Fabian, R. K. Kawakami, S. Roche, S. O. Valenzuela, *Nat. Nanotechnol.* **2021**, *16*, 856.
[16] Z. Zhang, P. Lin, Q. Liao, Z. Kang, H. Si, Y. Zhang, *Adv. Mater.* **2019**, *31*, 1806411.

[17] W. Ren, Y. Ouyang, P. Jiang, C. Yu, J. He, J. Chen, *Nano Lett.* **2021**, *21*, 2634.
[18] M. Yankowitz, Q. Ma, P. Jarillo-Herrero, B. J. LeRoy, *Nat. Rev. Phys.* **2019**, *1*, 112.
[19] Y. Jiang, S. Chen, W. Zheng, B. Zheng, A. Pan, *Light: Sci. Appl.* **2021**, *10*, 72.
[20] F. Bonaccorso, A. Lombardo, T. Hasan, Z. Sun, L. Colombo, A. C. Ferrari, *Mater. Today* **2012**, *15*, 564.
[21] K. S. Novoselov, V. I. Fal'ko, L. Colombo, P. R. Gellert, M. G. Schwab, K. Kim, *Nature* **2012**, *490*, 192.
[22] S. Z. Butler, S. M. Hollen, L. Cao, Y. Cui, J. A. Gupta, H. R. Gutierrez, T. F. Heinz, S. S. Hong, J. Huang, A. F. Ismach, E. Johnston-Halperin, M. Kuno, V. V. Plashnitsa, R. D. Robinson, R. S. Ruoff, S. Salahuddin, J. Shan, L. Shi, M. G. Spencer, M. Terrones, W. Windl, J. E. Goldberger, *ACS Nano* **2013**, *7*, 2898.
[23] G. R. Bhimanapati, Z. Lin, V. Meunier, Y. Jung, J. Cha, S. Das, D. Xiao, Y. Son, M. S. Strano, V. R. Cooper, L. Liang, S. G. Louie, E. Ringe, W. Zhou, S. S. Kim, R. R. Naik, B. G. Sumpter, H. Terrones, F. Xia, Y. Wang, J. Zhu, D. Akinwande, N. Alem, J. A. Schuller, R. E. Schaak, M. Terrones, J. A. Robinson, *ACS Nano* **2015**, *9*, 11509.
[24] A. L. Exarhos, D. A. Hopper, R. N. Patel, M. W. Doherty, L. C. Bassett, *Nat. Commun.* **2019**, *10*, 222.
[25] J. Y. Qin, R. Q. Jiang, M. Luo, T. T. Cheng, Y. X. Meng, Y. Z. Zu, J. Z. Zhang, J. C. Ho, C. H. Yu, J. H. Chu, *Infrared Phys. Technol.* **2024**, *137*, 105105.
[26] D. Zhang, P. Schoenherr, P. Sharma, J. Seidel, *Nat. Rev. Mater.* **2022**, *8*, 25.
[27] W. J. Liu, Y. Y. Yu, M. Peng, Z. H. Zheng, P. C. Jian, Y. Wang, Y. C. Zou, Y. M. Zhao, F. Wang, F. Wu, C. Q. Chen, J. N. Dai, P. Wang, W. D. Hu, *InfoMat* **2023**, *5*, e12470.
[28] A. Hwang, M. Park, Y. Park, Y. Shim, S. Youn, C. H. Lee, H. B. Jeong, H. Y. Jeong, J. Chang, K. Lee, G. Yoo, J. Heo, *Sci. Adv.* **2021**, *7*, eabj2521.
[29] X. Li, W. Chen, S. Zhang, Z. Wu, P. Wang, Z. Xu, H. Chen, W. Yin, H. Zhong, S. Lin, *Nano Energy* **2015**, *16*, 310.
[30] W. Song, J. Chen, Z. Li, X. Fang, *Adv. Mater.* **2021**, *33*, 2101059.
[31] Q. Li, C. Yang, L. Xu, S. Liu, S. Fang, L. Xu, J. Yang, J. Ma, Y. Li, B. Wu, R. Quhe, K. Tang, J. Lu, *Adv. Funct. Mater.* **2023**, *33*, 2214653.
[32] D. Sarkar, J. Tao, R. Ahsan, D. Yang, T. Orvis, S. Weng, F. Greer, J. Ravichandran, C. Sideris, R. Kapadia, *ACS Appl. Electron.* **2020**, *2*, 1997.
[33] H. Gamo, K. Tomioka, *IEEE Electron Device Lett.* **2020**, *41*, 1169.
[34] A. Ahmed, K. Chung, W. I. Park, G. C. Yi, *J. Inf. Disp.* **2024**, *25*, 75.
[35] Y. Meng, J. Feng, S. Han, Z. Xu, W. Mao, T. Zhang, J. S. Kim, I. Roh, Y. Zhao, D. H. Kim, Y. Yang, J. W. Lee, L. Yang, C.-W. Qiu, S. H. Bae, *Nat. Rev. Mater.* **2023**, *8*, 498.
[36] H. Bahmani Jalali, L. De Trizio, L. Manna, F. Di Stasio, *Chem. Soc. Rev.* **2022**, *51*, 9861.
[37] A. Rogalski, P. Martyniuk, M. Kopytko, *Appl. Phys. Rev.* **2017**, *4*, 031304.
[38] M. M. Desjardins, L. C. Contamin, M. R. Delbecq, M. C. Dartiailh, L. E. Bruhat, T. Cubaynes, J. J. Viennot, F. Mallet, S. Rohart, A. Thiaville, A. Cottet, T. Kontos, *Nat. Mater.* **2019**, *18*, 1060.
[39] R. M. Lutchyn, E. P. A. M. Bakkers, L. P. Kouwenhoven, P. Krogstrup, C. M. Marcus, Y. Oreg, *Nat. Rev. Mater.* **2018**, *3*, 52.
[40] C. B. Zota, D. Lindgren, L. E. Wernersson, E. Lind, *ACS Nano* **2015**, *9*, 9892.
[41] R. K. Singh, S. Singh, *Phys. Rev. B* **1989**, *39*, 671.
[42] T. T. Cheng, K. Zhang, M. Luo, Y. X. Meng, Y. Z. Zu, Y. J. Wang, P. Wang, C. H. Yu, *J. Infrared Millim. Waves* **2023**, *42*, 666.
[43] H. Zheng, J. Wang, J. Y. Huang, J. Wang, Z. Zhang, S. X. Mao, *Nano Lett.* **2013**, *13*, 6023.
[44] E. A. Anyebe, M. Kesaria, *Nano Sel.* **2020**, *2*, 688.
[45] A. Mazid Munshi, H. Weman, *Phys. Status Solidi RRL* **2013**, *7*, 713.
[46] K. Zheng, Z. Zhang, Y. Hu, P. Chen, W. Lu, J. Drennan, X. Han, J. Zou, *Nano Lett.* **2016**, *16*, 1787.
[47] A. Nikolaevich Klochkov, A. Nikolaevich Vinichenko, A. Alekseevich Samolyga, S. Mihailovich Ryndya, M. Viktorovich Poliakov, *N. Appl. Surf. Sci.* **2023**, *619*, 156722.
[48] J. E. Choi, J. Yoo, D. Lee, Y. J. Hong, T. Fukui, *Appl. Phys. Lett.* **2018**, *112*, 142101.
[49] H. Şahin, S. Cahangirov, M. Topsakal, E. Bekaroglu, E. Akturk, R. T. Senger, S. Ciraci, *Phys. Rev. B* **2009**, *80*, 155453.
[50] V. O. Özçelik, J. G. Azadani, C. Yang, S. J. Koester, T. Low, *Phys. Rev. B* **2016**, *94*, 035125.
[51] H. L. L. Zhuang, A. K. Singh, R. G. Hennig, *Phys. Rev. B* **2013**, *87*, 165415.
[52] C. J. Tong, H. Zhang, Y. N. Zhang, H. Liu, L. M. Liu, *J. Mater. Chem. A* **2014**, *2*, 17971.
[53] T. Suzuki, *Appl. Phys. Lett.* **2015**, *107*, 213105.
[54] M. C. Lucking, W. Xie, D. H. Choe, D. West, T. M. Lu, S. B. Zhang, *Phys. Rev. Lett.* **2018**, *120*, 086101.
[55] S. Ahmed, A. Jalil, S. Z. Ilyas, H. Mufti, S. Agathopoulos, *Mater. Sci. Semicond. Process.* **2021**, *134*, 106041.
[56] Y. Li, X. Ma, H. Bao, J. Zhou, F. Ma, J. Li, *Nano Res.* **2022**, *16*, 3443.
[57] M. Y. Ma, D. Han, N. K. Chen, D. Wang, X. B. Li, *Materials* **2022**, *15*, 7715.
[58] T. Akiyma, Y. Hasegawa, K. Nakamura, T. Ito, *Appl. Phys. Express* **2019**, *12*, 125501.
[59] D. L. Duong, S. J. Yun, Y. H. Lee, *ACS Nano* **2017**, *11*, 11803.
[60] S. J. Liang, B. Cheng, X. Cui, F. Miao, *Adv. Mater.* **2020**, *32*, 1903800.
[61] J. K. Qin, C. Wang, L. Zhen, L.-J. Li, C.-Y. Xu, Y. Chai, *Prog. Mater. Sci.* **2021**, *122*, 100856.
[62] A. Rogalski, *Opto-Electron. Rev.* **2024**, *30*, e140551.
[63] A. Koma, K. Sunouchi, T. Miyajima, *Microelectron. Eng.* **1984**, *2*, 129.
[64] A. Koma, *Thin Solid Films* **1992**, *216*, 72.
[65] H. Ryu, H. Park, J. H. Kim, F. Ren, J. Kim, G. H. Lee, S. J. Pearton, *Appl. Phys. Rev.* **2022**, *9*, 031305.
[66] X. Zhang, Y. Zhang, H. Yu, H. Zhao, Z. Cao, Z. Zhang, Y. Zhang, *Adv. Mater.* **2022**, *10*, 2207966.
[67] C. Zhao, Z. Li, T. Tang, J. Sun, W. Zhan, B. Xu, H. Sun, H. Jiang, K. Liu, S. Qu, Z. Wang, Z. Wang, *Prog. Quantum Electron.* **2021**, *76*, 100313.
[68] X. Zhang, T.-Y. Park, Y. Jia, H. Chang, T. K. Ng, B. S. Ooi, *Cryst. Growth Des.* **2023**, *23*, 3813.
[69] K. Nakada, A. Ishii, *Solid State Commun.* **2011**, *151*, 13.
[70] A. M. Munshi, D. L. Dheeraj, V. T. Fauske, D. C. Kim, A. T. van Helvoort, B. O. Fimland, H. Weman, *Nano Lett.* **2012**, *12*, 4570.
[71] D. G. Sangiovanni, R. Faccio, G. K. Gueorguiev, A. Kakanakova-Georgieva, *Phys. Chem. Chem. Phys.* **2022**, *25*, 829.
[72] H. Kum, D. Lee, W. Kong, H. Kim, Y. Park, Y. Kim, Y. Baek, S.-H. Bae, K. Lee, J. Kim, *Nat. Electron.* **2019**, *2*, 439.
[73] H. Y. Wang, Z. X. Li, D. Y. Li, P. Chen, L. Pi, X. Zhou, T. Y. Zhai, *Adv. Funct. Mater.* **2021**, *31*, 2103106.
[74] P. Wang, C. Jia, Y. Huang, X. Duan, *Matter* **2021**, *4*, 552.
[75] B. Zhao, Z. Wan, Y. Liu, J. Xu, X. Yang, D. Shen, Z. Zhang, C. Guo, Q. Qian, J. Li, R. Wu, Z. Lin, X. Yan, B. Li, Z. Zhang, H. Ma, B. Li, X. Chen, Y. Qiao, I. Shakir, Z. Almutairi, F. Wei, Y. Zhang, X. Pan, Y. Huang, Y. Ping, X. Duan, X. Duan, *Nature* **2021**, *591*, 385.
[76] X. T. Yu, X. Wang, F. F. Zhou, J. L. Qu, J. Song, *Adv. Funct. Mater.* **2021**, *31*, 2104260.
[77] P. S. Wu, L. Ye, L. Tong, P. Wang, Y. Wang, H. L. Wang, H. N. Ge, Z. Wang, Y. Gu, K. Zhang, Y. Y. Yu, M. Peng, F. Wang, M. Huang, P. Zhou, W. D. Hu, *Light: Sci. Appl.* **2022**, *11*, 6.
[78] F. Wang, T. Zhang, R. Z. Xie, A. N. Liu, F. X. Dai, Y. Chen, T. F. Xu, H. L. Wang, Z. Wang, L. Liao, J. L. Wang, P. Zhou, W. D. Hu, *Adv. Mater.* **2023**, *35*, 2307217.

[79] Y. Hinuma, H. Hayashi, Y. Kumagai, I. Tanaka, F. Oba, *Phys. Rev. B* **2017**, *96*, 094102.
[80] M. Shishkin, G. Kresse, *Phys. Rev. B* **2006**, *74*, 035101.
[81] C. Freysoldt, B. Grabowski, T. Hickel, J. Neugebauer, G. Kresse, A. Janotti, C. G. Van de Walle, *Rev. Mod. Phys.* **2014**, *86*, 253.
[82] S. Grimme, *J. Comput. Chem.* **2006**, *27*, 1787.
[83] S. Grimme, J. Antony, S. Ehrlich, H. Krieg, *J. Chem. Phys.* **2010**, *132*, 154104.
[84] A. Tkatchenko, M. Scheffler, *Phys. Rev. Lett.* **2009**, *102*, 073005.
[85] Y. Zhao, D. Truhlar, *Acc. Chem. Res.* **2008**, *41*, 157.
[86] A. D. Becke, *J. Chem. Phys.* **2014**, *140*, 18A301.
[87] F. Oba, Y. Kumagai, *Appl. Phys. Express* **2018**, *11*, 060101.
[88] J. M. del Campo, J. L. Gazquez, S. B. Trickey, A. Vela, *J. Chem. Phys.* **2012**, *136*, 104108.
[89] S. Grimme, *Wires Comput. Mol. Sci.* **2011**, *1*, 211.
[90] W. Hu, J. Yang, *Comput. Mater. Sci.* **2016**, *112*, 518.
[91] S. Grimme, *J. Comput. Chem.* **2004**, *25*, 1463.
[92] S. Grimme, S. Ehrlich, L. Goerigk, *J. Comput. Chem.* **2011**, *32*, 1456.
[93] J. Klimes, A. Michaelides, *J. Chem. Phys.* **2012**, *137*, 120901.
[94] J. Hermann, R. A. DiStasio Jr., A. Tkatchenko, *Chem. Rev.* **2017**, *117*, 4714.
[95] K. Lejaeghere, G. Bihlmayer, T. Bjorkman, P. Blaha, S. Blugel, V. Blum, D. Caliste, I. E. Castelli, S. J. Clark, A. Dal Corso, S. de Gironcoli, T. Deutsch, J. K. Dewhurst, I. Di Marco, C. Draxl, M. Dulak, O. Eriksson, J. A. Flores-Livas, K. F. Garrity, L. Genovese, P. Giannozzi, M. Giantomassi, S. Goedecker, X. Gonze, O. Granas, E. K. Gross, A. Gulans, F. Gygi, D. R. Hamann, P. J. Hasnip, et al., *Science* **2016**, *351*, aad3000.
[96] S. Lehtola, C. Steigemann, M. J. T. Oliveira, M. A. L. Marques, *SoftwareX* **2018**, *7*, 1.
[97] D. Liang, J. Du, X. P. A. Gao, *J. Mater. Sci. Technol.* **2015**, *31*, 542.
[98] C. Jia, Z. Lin, Y. Huang, X. Duan, *Chem. Rev.* **2019**, *119*, 9074.
[99] T. F. Xu, H. L. Wang, X. Y. Chen, M. Luo, L. L. Zhang, Y. M. Wang, F. S. Chen, C. X. Shan, C. H. Yu, *Nanotechnology* **2020**, *31*, 294004.
[100] X. Wang, J. Choi, J. Yoo, Y. J. Hong, *Nano Converg.* **2023**, *10*, 39.
[101] Y. J. Hong, R. K. Saroj, W. I. Park, G. C. Yi, *APL Mater.* **2021**, *9*, 060907.
[102] Y. J. Hong, T. Fukui, *ACS Nano* **2011**, *5*, 7576.
[103] Y. J. Hong, W. H. Lee, Y. Wu, R. S. Ruoff, T. Fukui, *Nano Lett.* **2012**, *12*, 1431.
[104] M. A. Baboli, A. Abrand, R. A. Burke, A. Fedorenko, T. S. Wilhelm, S. J. Polly, M. Dubey, S. M. Hubbard, P. K. Mohseni, *Nanoscale Adv.* **2021**, *3*, 2802.
[105] M. A. Baboli, M. A. Slocum, H. Kum, T. S. Wilhelm, S. J. Polly, S. M. Hubbard, P. K. Mohseni, *CrystEngComm* **2019**, *21*, 602.
[106] X. Yuan, D. Pan, Y. Zhou, X. Zhang, K. Peng, B. Zhao, M. Deng, J. He, H. H. Tan, C. Jagadish, *Appl. Phys. Rev.* **2021**, *8*, 021302.
[107] J. Meyer-Holdt, T. Kanne, J. E. Sestoft, A. Gejl, L. Zeng, E. Johnson, E. Olsson, J. Nygard, P. Krogstrup, *Nanotechnology* **2016**, *27*, 365603.
[108] E. A. Anyebe, I. Sandall, Z. M. Jin, A. M. Sanchez, M. K. Rajpalke, T. D. Veal, Y. C. Cao, H. D. Li, R. Harvey, Q. D. Zhuang, *Sci. Rep.* **2017**, *7*, 46110.
[109] P. K. Mohseni, A. Behnam, J. D. Wood, C. D. English, J. W. Lyding, E. Pop, X. Li, *Nano Lett.* **2013**, *13*, 1153.
[110] A. G. S. Vilasam, S. Adhikari, B. Gupta, S. Balendhran, N. Higashitarumizu, J. Tournet, L. Li, A. Javey, K. B. Crozier, S. Karuturi, C. Jagadish, H. H. Tan, *Nanotechnology* **2023**, *34*, 495601.
[111] J. Wallentin, D. Kriegner, J. Stangl, M. T. Borgstrom, *Nano Lett.* **2014**, *14*, 1707.
[112] Q. D. Zhuang, E. A. Anyebe, A. M. Sanchez, M. K. Rajpalke, T. D. Veal, A. Zhukov, B. J. Robinson, F. Anderson, O. Kolosov, V. Fal'ko, *Nanoscale Res. Lett.* **2014**, *9*, 321.
[113] E. A. Anyebe, M. Kesaria, A. M. Sanchez, Q. Zhuang, *Appl. Phys. A* **2020**, *126*, 427.
[114] E. A. Anyebe, A. M. Sanchez, S. Hindmarsh, X. Chen, J. Shao, M. K. Rajpalke, T. D. Veal, B. J. Robinson, O. Kolosov, F. Anderson, R. Sundaram, Z. M. Wang, V. Falko, Q. Zhuang, *Nano Lett.* **2015**, *15*, 4348.
[115] P. K. Mohseni, A. Behnam, J. D. Wood, X. Zhao, K. J. Yu, N. C. Wang, A. Rockett, J. A. Rogers, J. W. Lyding, E. Pop, X. Li, *Adv. Mater.* **2014**, *26*, 3755.
[116] Y. Tchoe, J. Jo, M. Kim, G.-C. Yi, *NPG Asia Mater* **2015**, *7*, e206.
[117] Y. J. Hong, J. W. Yang, W. H. Lee, R. S. Ruoff, K. S. Kim, T. Fukui, *Adv. Mater.* **2013**, *25*, 6847.
[118] Y. Tchoe, J. Jo, H. Kim, H. Kim, H. Baek, K. Lee, D. Yoo, W. J. Choi, M. Kim, G.-C. Yi, *NPG Asia Mater.* **2021**, *13*, 33.
[119] X. Wang, X. H. Li, C. Jiang, C. T. A. Brown, J. Q. Ning, K. Zhang, Q. Yu, X. T. Ge, Q. J. Wang, Z. Y. Zhang, *NPJ 2D Mater.* **2020**, *4*, 27.
[120] K. Xin, L. Li, Z. Zhou, C. Zhang, J. Yang, H.-X. Deng, J. Zhang, J. Liu, K. Liu, C. Liu, F. Liu, Z. Wei, S. Zhai, *Nat. Synth.* **2024**, https://doi.org/10.1038/s44160-024-00562-0.
[121] C. Jiang, X. Wang, H. Wang, S. Wang, L. Qin, J. Liu, Z. Zhang, *Adv. Photonics Res.* **2021**, *3*, 2100183.
[122] J. X. Dai, T. Z. Yang, Z. T. Jin, Y. L. Zhong, X. Y. Hu, J. Y. Zou, W. G. Xu, T. Li, Y. X. Lin, X. Zhang, L. Zhou, *Nano Res.* **2022**, *11*, 9954.
[123] P. Tsipas, D. Tsoutsou, S. Fragkos, R. Sant, C. Alvarez, H. Okuno, G. Renaud, R. Alcotte, T. Baron, A. Dimoulas, *ACS Nano* **2018**, *12*, 1696.
[124] F. Arciprete, J. E. Boschker, S. Cecchi, E. Zallo, V. Bragaglia, R. Calarco, *Adv. Mater. Interfaces* **2021**, *9*, 2101556.
[125] R. Frisenda, E. Navarro-Moratalla, P. Gant, D. Perez De Lara, P. Jarillo-Herrero, R. V. Gorbachev, A. Castellanos-Gomez, *Chem. Soc. Rev.* **2018**, *47*, 53.
[126] T. F. Schranghamer, M. Sharma, R. Singh, S. Das, *Chem. Soc. Rev.* **2021**, *50*, 11032.
[127] A. J. Watson, W. Lu, M. H. D. Guimarães, M. Stöhr, *2D Mater.* **2021**, *8*, 032001.
[128] H. W. Guo, Z. Hu, Z. B. Liu, J. G. Tian, *Adv. Funct. Mater.* **2020**, *31*, 2007810.
[129] S. Chuang, R. Kapadia, H. Fang, T. Chia Chang, W.-C. Yen, Y.-L. Chueh, A. Javey, *Appl. Phys. Lett.* **2013**, *102*, 242101.
[130] H. Takita, N. Hashimoto, C. T. Nguyen, M. Kudo, M. Akabori, T.-K. Suzuki, *Appl. Phys. Lett.* **2010**, *97*, 012102.
[131] C. Thanh Nguyen, H.-A. Shih, M. Akabori, T.-k. Suzuki, *Appl. Phys. Lett.* **2012**, *100*, 232103.
[132] S. Fan, Q. A. Vu, M. D. Tran, S. Adhikari, Y. H. Lee, *2D Mater.* **2020**, *7*, 022005.
[133] Y. Liu, J. Guo, E. Zhu, P. Wang, V. Gambin, Y. Huang, X. Duan, *ACS Nano* **2019**, *13*, 847.
[134] Y. Liu, J. Guo, W. Song, P. Wang, V. Gambin, Y. Huang, X. Duan, *Small Struct.* **2020**, *2*, 2000039.
[135] K. H. Kim, D. S. Um, H. Lee, S. Lim, J. Chang, H. C. Koo, M.-W. Oh, H. Ko, H. j. Kim, *ACS Nano* **2013**, *7*, 9106.
[136] D. S. Um, Y. Lee, S. Lim, J. Park, W. C. Yen, Y. L. Chueh, H. J. Kim, H. Ko, *ACS Appl. Mater. Interfaces* **2016**, *8*, 26105.
[137] Y. Liu, Z. Li, F. B. Atar, H. Muthuganesan, B. Corbett, L. Wang, *ACS Appl. Mater. Interfaces* **2024**, *16*, 10996.
[138] S. Fan, X. Li, A. Mondal, W. Wang, Y. H. Lee, *2D Mater.* **2024**, *11*, 033002.
[139] H. Liu, Q. H. Thi, P. Man, X. Chen, T. Chen, L. W. Wong, S. Jiang, L. Huang, T. Yang, K. H. Leung, T. T. Leung, S. Gao, H. Chen, C. S. Lee, M. Kan, J. Zhao, Q. Deng, T. H. Ly, *Adv. Mater.* **2023**, *35*, 2210503.
[140] A. V. Velichko, Z. R. Kudrynskyi, D. M. Di Paola, O. Makarovsky, M. Kesaria, A. Krier, I. C. Sandall, C. H. Tan, Z. D. Kovalyuk, A. Patanè, *Appl. Phys. Lett.* **2016**, *109*, 182115.
[141] W. D. Hu, Z. H. Ye, L. Liao, H. L. Chen, L. Chen, R. J. Ding, L. He, X. S. Chen, W. Lu, *Opt. Lett.* **2014**, *39*, 5184.

[142] Y. F. Chen, Y. Wang, Z. Wang, Y. Gu, Y. Ye, X. L. Chai, J. F. Ye, Y. Chen, R. Z. Xie, Y. Zhou, Z. G. Hu, Q. Li, L. L. Zhang, F. Wang, P. Wang, J. S. Miao, J. L. Wang, X. S. Chen, W. Lu, P. Zhou, W. D. Hu, *Nat. Electron.* **2021**, *4*, 357.
[143] N. Gupta, S. Wang, N. Higashitarumizu, V. Wang, K. Lee, C. Park, A. Javey, *Sci. Adv.* **2023**, *9*, eadi9384.
[144] J. Bullock, M. Amani, J. Cho, Y.-Z. Chen, G. H. Ahn, V. Adinolfi, V. R. Shrestha, Y. Gao, K. B. Crozier, Y.-L. Chueh, A. Javey, *Nat. Photonics* **2018**, *12*, 601.
[145] J. Deng, L. Zong, W. Bao, M. Zhu, F. Liao, Z. Guo, Y. Xie, B. Lu, J. Wan, J. Zhu, R. Peng, Y. Chen, *Adv. Opt. Mater.* **2019**, *7*, 1901039.
[146] J. S. Miao, W. D. Hu, N. Guo, Z. Y. Lu, X. Q. Liu, L. Liao, P. P. Chen, T. Jiang, S. W. Wu, J. C. Ho, L. Wang, X. S. Chen, W. Lu, *Small* **2015**, *11*, 936.
[147] H. N. Ge, R. Z. Xie, J. X. Guo, Q. Li, Y. Y. Yu, J. L. He, F. Wang, P. Wang, W. D. Hu, *Acta Phys. Sin.* **2022**, *71*, 110703.
[148] H. N. Ge, R. Z. Xie, Y. F. Chen, P. Wang, Q. Li, Y. Gu, J. X. Guo, J. L. He, F. Wang, W. D. Hu, *Opt. Express* **2021**, *29*, 22823.
[149] E. Barrigon, M. Heurlin, Z. Bi, B. Monemar, L. Samuelson, *Chem. Rev.* **2019**, *119*, 9170.
[150] H. H. Fang, W. D. Hu, P. Wang, N. Guo, W. J. Luo, D. S. Zheng, F. Gong, M. Luo, H. Z. Tian, X. T. Zhang, C. Luo, X. Wu, P. P. Chen, L. Liao, A. Pan, X. S. Chen, W. Lu, *Nano Lett.* **2016**, *16*, 6416.
[151] W. J. Luo, Q. C. Weng, M. S. Long, P. Wang, F. Gong, H. H. Fang, M. Luo, W. J. Wang, Z. Wang, D. S. Zheng, W. D. Hu, X. S. Chen, W. Lu, *Nano Lett.* **2018**, *18*, 5439.
[152] F. X. Dai, F. Wang, H. N. Ge, R. Z. Xie, R. Q. Jiang, H. R. Shi, H. Liu, G. J. Hu, L. Shen, T. X. Li, W. D. Hu, *IEEE Electron Device Lett.* **2024**, *45*, 16.
[153] Q. Li, F. Wang, P. Wang, L. L. Zhang, J. L. He, L. Chen, P. Martyniuk, A. Rogalski, X. S. Chen, W. Lu, W. D. Hu, *IEEE Trans. Electron Devices* **2020**, *67*, 542.
[154] W. D. Hu, X. S. Chen, Z. H. Ye, A. L. Feng, F. Yin, B. Zhang, L. Liao, W. Lu, *J. Sel. Top. Quantum Electron.* **2013**, *19*, 1.
[155] J. Svensson, P. Olausson, H. Menon, S. Lehmann, E. Lind, M. Borg, *Nano Lett.* **2023**, *23*, 4756.
[156] N. Youngblood, M. Li, *Nanophotonics* **2016**, *6*, 1205.
[157] I. Žutić, J. Fabian, S. Das Sarma, *Rev. Mod. Phys.* **2004**, *76*, 323.
[158] X. Zhang, M. Yang, L. Chen, X. Zhou, *J. Mater. Res.* **2021**, *37*, 479.
[159] H. Li, Y. Liu, Z. Bai, J. Xiong, F. Liu, G. Zhou, T. Qing, S. Zhang, J. Lu, *Phys. Lett. A* **2022**, *433*, 128029.
[160] M. Q. Xie, Y. Li, X. H. Liu, X. A. Li, *Appl. Surf. Sci.* **2022**, *591*, 153198.
[161] X. F. Liu, Z. J. Luo, X. Zhou, J. M. Wei, Y. Wang, X. Guo, B. Lv, Z. Ding, *Chin. Phys. B* **2019**, *28*, 8.
[162] Y. J. Chen, B. N. Jia, X. N. Guan, L. H. Han, L. Y. Wu, P. F. Guan, P. F. Lu, *Appl. Surf. Sci.* **2022**, *586*, 152799.
[163] J. Lu, Z. Q. Fan, J. Gong, X. W. Jiang, *Phys. Chem. Chem. Phys.* **2017**, *19*, 20121.
[164] W. Yu, J. Li, Y. Wu, J. Lu, Y. Zhang, *Phys. Chem. Chem. Phys.* **2023**, *25*, 10769.
[165] M. T. Yu, S. Moayedpour, S. Y. Yang, D. Dardzinski, C. Z. Wu, V. S. Pribiag, N. Marom, *Phys. Rev. Mater.* **2021**, *5*, 064606.
[166] S. Y. Yang, D. Dardzinski, A. Hwang, D. I. Pikulin, G. W. Winkler, N. Marom, *Phys. Rev. Mater.* **2021**, *5*, 084204.
[167] F. Ning, D. Wang, Y.-X. Feng, L.-M. Tang, Y. Zhang, K.-Q. Chen, *J. Mater. Chem. C* **2017**, *5*, 9429.
[168] Z. Santos, P. P. Dholabhai, *Comput. Mater. Sci.* **2021**, *194*, 110426.
[169] Y. S. Kim, K. Hummer, G. Kresse, *Phys. Rev. B* **2009**, *80*, 073005.
[170] Y. Hinuma, A. Grüneis, G. Kresse, F. Oba, *Phys. Rev. B* **2014**, *90*, 15.
[171] K. Berland, V. R. Cooper, K. Lee, E. Schroder, T. Thonhauser, P. Hyldgaard, B. I. Lundqvist, *Rep. Prog. Phys.* **2015**, *78*, 066501.
[172] F. Ning, S. Z. Chen, Y. Zhang, G. H. Liao, P. Y. Tang, Z. L. Li, L. M. Tang, *Appl. Surf. Sci.* **2019**, *496*, 143629.
[173] T. Akiyama, T. Kawamura, T. Ito, *Appl. Phys. Lett.* **2021**, *118*, 023101.
[174] D. P. Andrade, R. H. Miwa, G. P. Srivastava, *Phys. Rev. B* **2011**, *84*, 165322.
[175] B. Sa, Z. Sun, B. Wu, *Nanoscale* **2016**, *8*, 1169.
[176] S. S. Lin, *J. Phys. Chem. C* **2012**, *116*, 3951.
[177] L. Qin, Z. H. Zhang, Z. Jiang, K. Fan, W. H. Zhang, Q. Y. Tang, H. N. Xia, F. Meng, Q. Zhang, L. Gu, D. West, S. Zhang, Y. S. Fu, *ACS Nano* **2021**, *15*, 8184.
[178] C. Jin, E. Y. Ma, O. Karni, E. C. Regan, F. Wang, T. F. Heinz, *Nat. Nanotechnol.* **2018**, *13*, 994.
[179] S. Ponce, W. Li, S. Reichardt, F. Giustino, *Phys. Rev. B* **2020**, *83*, 036501.
[180] Y. Liu, A. Luchini, S. Marti-Sanchez, C. Koch, S. Schuwalow, S. A. Khan, T. Stankevic, S. Francoual, J. R. L. Mardegan, J. A. Krieger, V. N. Strocov, J. Stahn, C. A. F. Vaz, M. Ramakrishnan, U. Staub, K. Lefmann, G. Aeppli, J. Arbiol, P. Krogstrup, *ACS Appl. Mater. Interfaces* **2020**, *12*, 8780.
[181] Z. Zhang, X. Yang, K. Liu, R. Wang, *Adv. Sci.* **2022**, *9*, 2105201.
[182] E. A. Anyebe, M. Kesaria, *Nano Select* **2021**, *2*, 688.
[183] W. Liu, Y. Yu, M. Peng, Z. Zheng, P. Jian, Y. Wang, Y. Zou, Y. Zhao, F. Wang, F. Wu, *InfoMat* **2023**, *5*, e12470.
[184] F. Lu, H. Wang, M. Zeng, L. Fu, *iScience* **2022**, *25*, 103835.
[185] J. Dai, T. Yang, Z. Jin, Y. Zhong, X. Hu, J. Zou, W. Xu, T. Li, Y. Lin, X. Zhang, L. Zhou, *Nano Res.* **2022**, *15*, 9954.
[186] J. Ji, H. M. Kwak, J. Yu, S. Park, J. H. Park, H. Kim, S. Kim, S. Kim, D. S. Lee, H. S. Kum, *Nano Converg* **2023**, *10*, 19.
[187] S. Manzo, P. J. Strohbeen, Z. H. Lim, V. Saraswat, D. Du, S. Xu, N. Pokharel, L. J. Mawst, M. S. Arnold, J. K. Kawasaki, *Nat. Commun.* **2022**, *13*, 4014.
[188] D. Du, T. Jung, S. Manzo, Z. LaDuca, X. Zheng, K. Su, V. Saraswat, J. McChesney, M. S. Arnold, J. K. Kawasaki, *Nano Lett.* **2022**, *22*, 8647.
[189] I. A. Kinloch, J. Suhr, J. Lou, R. J. Young, P. M. Ajayan, *Science* **2018**, *362*, 547.
[190] M. G. Zhu, J. Si, Z. Zhang, L. M. Peng, *Adv. Mater.* **2018**, *30*, 1707068.
[191] Y. Bai, H. Yue, J. Wang, B. Shen, S. Sun, S. Wang, H. Wang, X. Li, Z. Xu, R. Zhang, F. Wei, *Science* **2020**, *369*, 1104.
[192] A. D. Franklin, M. C. Hersam, H. P. Wong, *Science* **2022**, *378*, 726.
[193] G. Hills, C. Lau, A. Wright, S. Fuller, M. D. Bishop, T. Srimani, P. Kanhaiya, R. Ho, A. Amer, Y. Stein, D. Murphy, Arvind, A. C., M. M. Shulaker, *Nature* **2019**, *572*, 595.
[194] L. Liu, J. Han, L. Xu, J. Zhou, C. Zhao, S. Ding, H. Shi, M. Xiao, L. Ding, Z. Ma, C. Jin, Z. Zhang, L. M. Peng, *Science* **2020**, *368*, 850.
[195] P. K. Mohseni, G. Lawson, C. Couteau, G. Weihs, A. Adronov, R. R. LaPierre, *Nano Lett.* **2008**, *8*, 4075.
[196] P. K. Mohseni, G. Lawson, A. Adronov, R. R. LaPierre, *IEEE J. Sel. Top. Quantum Electron.* **2011**, *17*, 1070.
[197] C. S. Chang, K. S. Kim, B.-I. Park, J. Choi, H. Kim, J. Jeong, M. Barone, N. Parker, S. Lee, X. Zhang, K. Lu, J. M. Suh, J. Kim, D. Lee, N. M. Han, M. Moon, Y. S. Lee, D.-H. Kim, D. G. Schlom, Y. J. Hong, J. Kim, *Sci. Adv.* **2023**, *9*, eadj5379.
[198] I. Roh, S. H. Goh, Y. Meng, J. S. Kim, S. Han, Z. Xu, H. E. Lee, Y. Kim, S.-H. Bae, *Nano Converg.* **2023**, *10*, 20.
[199] Q. Chen, K. Yang, M. Liang, J. Kang, X. Yi, J. Wang, J. Li, Z. Liu, *Nano Converg.* **2023**, *10*, 39.
[200] B.-I. Park, J. Kim, K. Lu, X. Zhang, S. Lee, J. M. Suh, D.-H. Kim, H. Kim, J. Kim, *Nano Lett.* **2024**, *24*, 2939.
[201] Y. Kim, S. S. Cruz, K. Lee, B. O. Alawode, C. Choi, Y. Song, J. M. Johnson, C. Heidelberger, W. Kong, S. Choi, K. Qiao, I. Almansouri, E. A. Fitzgerald, J. Kong, A. M. Kolpak, J. Hwang, J. Kim, *Nature* **2017**, *544*, 340.
[202] J. Wu, F. Liu, M. Sasase, K. Ienaga, Y. Obata, R. Yukawa, K. Horiba, H. Kumigashira, S. Okuma, T. Inoshita, H. Hosono, *Sci. Adv.* **2019**, *5*, eaax9989.

[203] N. H. Vu, H. Van Le, T. B. Phan, T. T. Nguyen, N. Thoai, T. M. Cao, *J. Phys. Chem. C* **2020**, *124*, 8958.
[204] V. Gupta, R. Jain, Y. Ren, X. S. Zhang, H. F. Alnaser, A. Vashist, V. V. Deshpande, D. A. Muller, D. Xiao, T. D. Sparks, D. C. Ralph, *Nano Lett.* **2022**, *22*, 7166.
[205] M. Stohr, T. Van Voorhis, A. Tkatchenko, *Chem. Soc. Rev.* **2019**, *48*, 4118.
[206] M. Dion, H. Rydberg, E. Schroder, D. C. Langreth, B. I. Lundqvist, *Phys. Rev. Lett.* **2004**, *92*, 246401.
[207] G. Roman-Perez, J. M. Soler, *Phys. Rev. Lett.* **2009**, *103*, 096102.
[208] K. Lee, É. D. Murray, L. Kong, B. I. Lundqvist, D. C. Langreth, *Phys. Rev. B* **2010**, *82*, 8.
[209] M. Cerezo, G. Verdon, H.-Y. Huang, L. Cincio, P. J. Coles, *Nat. Comput. Sci.* **2022**, *2*, 567.
[210] P. Verma, D. G. Truhlar, *Trends Chem* **2020**, *2*, 302.
[211] J. Schmidt, M. R. G. Marques, S. Botti, M. A. L. Marques, *Npj Comput. Mater.* **2019**, *5*, 83.
[212] X. Wang, H. Wang, Q. Luo, J. Yang, *J. Chem. Phys.* **2022**, *157*, 074304.
[213] C. C. Johnson, T. Quackenbush, T. Sorensen, D. Wingate, M. D. Killpack, *Front. Robot AI* **2021**, *8*, 654398.
[214] M. Burkle, U. Perera, F. Gimbert, H. Nakamura, M. Kawata, Y. Asai, *Phys. Rev. Lett.* **2021**, *126*, 177701.
[215] Y. LeCun, Y. Bengio, G. Hinton, *Nature* **2015**, *521*, 436.
[216] T. Xie, J. C. Grossman, *Phys. Rev. Lett.* **2018**, *120*, 086101.
[217] A. Merchant, S. Batzner, S. S. Schoenholz, M. Aykol, G. Cheon, E. D. Cubuk, *Nature* **2023**, *624*, 80.
[218] X. Qian, R. G. Yang, *Mater. Sci. Eng. R* **2021**, *146*, 100642.
[219] N. Marzari, A. Ferretti, C. Wolverton, *Nat. Mater.* **2021**, *20*, 736.
[220] G. Wetzstein, A. Ozcan, S. Gigan, S. Fan, D. Englund, M. Soljacic, C. Denz, D. A. B. Miller, D. Psaltis, *Nature* **2020**, *588*, 39.
[221] R. Hu, W. Lei, H. M. Yuan, S. H. Han, H. J. Liu, *Nanomaterials* **2022**, *12*, 13.
[222] H. Li, Z. Wang, N. Zou, M. Ye, R. Xu, X. Gong, W. Duan, Y. Xu, *Nat. Comput. Sci.* **2022**, *2*, 367.
[223] Y. Zhang, C. Ling, *Npj Comput. Mater.* **2018**, *4*, 25.
[224] Z. Li, J. R. Kermode, A. De Vita, *Phys. Rev. Lett.* **2015**, *114*, 096405.
[225] Z. Guo, P. Roy Chowdhury, Z. Han, Y. Sun, D. Feng, G. Lin, X. Ruan, *Npj Comput. Mater.* **2023**, *9*, 95.

Tiantian Cheng is currently pursuing her Ph.D. degree at the School of Microelectronics and School of Integrated Circuits, School of Information Science and Technology, Nantong University, China. Her research centers on low-dimensional semiconductor materials and devices, primarily focusing on exploring and innovating barrier engineering techniques to enhance the performance of infrared photodetectors.

Man Luo is working as a lecturer in the School of Microelectronics and the School of Integrated Circuits at Nantong University. She received her B.S. degree from the Hubei Normal University in 2014 and her Ph.D. degree from the Shanghai Institute of Technical Physics of the Chinese Academy of Sciences in 2019. Her research interests mainly focus on nanomaterials-based photoconductive/photovoltaic photodetectors, field-effect transistors, etc.

Johnny C. Ho is a Professor of Materials Science and Engineering at the City University of Hong Kong. He received his B.S. degree in Chemical Engineering and his M.S. and Ph.D. degrees in Materials Science and Engineering from the University of California, Berkeley, in 2002, 2005, and 2009, respectively. From 2009–2010, he was a postdoctoral research fellow in the Nanoscale Synthesis and Characterization Group at Lawrence Livermore National Laboratory. His research interests focus on nanoscale materials' synthesis, characterization, integration, and device applications for various technological applications, including nanoelectronics, sensors, and energy harvesting.

Chenhui Yu obtained his Ph.D. in Microelectronics and Solid-State Electronics from the Shanghai Institute of Technical Physics (SITP), Chinese Academy of Sciences (CAS), in 2007. He is a Full Professor and Doctoral Supervisor at the School of Microelectronics and School of Integrated Circuits, Nantong University, China. He has authored or co-authored over 70 peer-reviewed scholarly articles. His research endeavors are primarily dedicated to micro and nano semiconductor devices, explicitly emphasizing their design and rigorous performance evaluation.